December 2020

Multilayered Transmission Lines, Antennas and Phased Arrays with Structurally Integrated Control Electronics Using Additive Manufacturing

Merve Kacar
University of South Florida

Follow this and additional works at: https://digitalcommons.usf.edu/etd

Part of the Electrical and Computer Engineering Commons

Scholar Commons Citation

Kacar, Merve, "Multilayered Transmission Lines, Antennas and Phased Arrays with Structurally Integrated Control Electronics Using Additive Manufacturing" (2020). *USF Tampa Graduate Theses and Dissertations.*
https://digitalcommons.usf.edu/etd/9540

This Dissertation is brought to you for free and open access by the USF Graduate Theses and Dissertations at Digital Commons @ University of South Florida. It has been accepted for inclusion in USF Tampa Graduate Theses and Dissertations by an authorized administrator of Digital Commons @ University of South Florida. For more information, please contact scholarcommons@usf.edu.

Multilayered Transmission Lines, Antennas and Phased Arrays with Structurally Integrated

Control Electronics Using Additive Manufacturing

by

Merve Kacar

A dissertation submitted in partial fulfillment
of the requirements for the degree of
Doctor of Philosophy
Department of Electrical Engineering
College of Engineering
University of South Florida

Major Professor: Gokhan Mumcu, Ph.D.
Kenneth H. Church, Ph.D.
Jing Wang, Ph.D.
Thomas M. Weller, Ph.D.
Ying Zhong, Ph.D.

Date of Approval:
November 24, 2020

Keywords: 3D printing, microstrip antennas, antenna arrays, packaging

Dedication

To my family and my beloved.

Acknowledgments

approval of the work in Chapter 5. Also, I would like to thank to Nanotechnology Research and Education Center (NREC) of University of South Florida and Patrick Rondomanski for the SEM images used in this chapter.

Table of Contents

List of Tables

List of Figures

Abstract

This dissertation presents high-performance transmission lines, antennas, and phased arrays with novel packaging techniques by harnessing design flexibilities of additive manufacturing (AM). AM enables realizing multilayered RF electronics with complex geometrical structures that are not practical using conventional fabrication methods. Design flexibilities offered by AM as customized dielectric shapes/thicknesses, dielectric properties, metallization on conformal surfaces, and structural packaging are harnessed for multilayered RF applications. Although several works demonstrated the viability of AM for antenna realizations, its capability for addressing the needs of wideband, high radiation efficiency antenna systems packaged with active RF circuit components remains relatively unexplored. The first major contribution of this dissertation is the 3D printed wideband high-efficiency dual-polarized stacked patch antenna with embedded Monolithic Microwave Integrated Circuit (MMIC) switch. Specifically, dual-polarized antenna bandwidth is enhanced to cover the entire Ku-band by resorting to stacked patch layers, customizing substrate thicknesses, and infill ratios. Switch integration to select polarization is performed with 3D vertical transitions to achieve high return loss and small packaging. To retain a high radiation efficiency and enable future antenna array applications, a detailed investigation is also carried out to maximize the performance of microstrip feed lines by adjusting the substrate thickness, infill ratios, and deposition directions. The presented Ku-band antenna consists of five conductive and eight dielectric layers realized with a single AM platform and offers state-of-the-art performance. Specifically, to the best of our knowledge, the dissertation demonstrates the lowest attenuation in the literature for a fully printed microstrip line with 0.25 dB/cm measured insertion loss at 18 GHz. The antenna operates with more than 80% radiation efficiency and 45% impedance bandwidth. The antenna retains a

low cross-polarization ratio of 20 dB due to 3D feed line transitions and symmetric location of the embedded switch with respect to the antenna feed points.

Wideband aperture-patch antenna using DDM can be extended to phased array antennas installed on small or conformal platforms, which requires low back radiation and structurally integrated electronics compared to traditional bulky packaging. The second major contribution of this dissertation the demonstration of an X-band phased array antenna element with an embedded cavity and a MMIC phase shifter. Printing direction should be from base to the antenna to allow for printing on planar/conformal platforms. The cavity is embedded under the coupling aperture to increase the front-to-back ratio. A MMIC phase shifter in QFN package is fully embedded inside the substrate for packaging within a small unit cell. For characterization, the embedded microstrip feed line is transitioned to exposed CPW using selective FDM technique. The antenna exhibits 81% radiation efficiency (excluding IC loss) and 23% impedance matching bandwidth without the phase shifter. Embedded cavity over the coupling aperture of the patch antenna increases the front-to-back ratio to >20 dB. Return loss of the antenna with phase shifter is more than 10 dB within the operating bandwidth for different phase shifter states. The phased array antenna element is suitable for half-wavelength spacing. The design is implemented to a $2{\times}2$ sub-array with the addition of layers and shift registers to perform the signal, control, and bias line routing.

Microdispensed transmission lines (TLs) are known to show high conductor losses at microwave frequencies due to the low conductivity of silver inks and pastes, non-uniform cross-sections, and high surface roughness. Recently, laser micromachining has been introduced as a technique to improve the conductivity of coplanar waveguide (CPW). By laser micromachining the slots of the CPW, smoother, and highly conductive signal trace and ground plane edges have been obtained and shown to enhance effective conductivity. So far, this enhancement has only been shown with CPW. Since conductor loss depends on the TL type and geometry, the effect of laser micromachining on other TL types should be investigated. The third major contribution of this dissertation is the demonstration of laser micromachining for microstrip and grounded coplanar waveguide (GCPW) for the first time, and improvement of their conductivities within the 1 GHz –

30 GHz frequency range. Specifically, laser micromachining is shown to decrease insertion loss at 30 GHz by 0.18 dB/cm and 0.29 dB/cm for the microstrip and GCPW, respectively, when the TLs are over a 254 micrometer thick substrate 3.6 dielectric constant. Effective conductivity of laser micromachined microstrip line and GCPW are extracted as 5 MS/m and 12.5 MS/m at 30 GHz, respectively. It is shown that GCPW benefits from laser micromachining the most due to higher current concentration at the signal trace edges. Narrower lines are also shown to improve the most with laser micromachining.

Chapter 1: Introduction

Additive manufacturing (AM) is the fabrication process of building an object layer by layer from a CAD file. With the development of high precision, multimaterial machines, AM provides many advantages and design flexibilities for RF and antenna engineers [1]. For instance, complex geometries that are not practical with traditional fabrication techniques can be fabricated easily using AM. To use traditional fabrication techniques, a complex structure should be split into many parts, drilled or laser-machined, and assembled with screws. AM provides one-piece (monolithic) realization and increases accuracy for high frequency devices. AM techniques such as stereolithography (SLA) can be used to achieve lightweight antennas. For multilayer/multi-material structures, AM offers design flexibilities in terms of custom layer thicknesses, custom shapes such as inclined surfaces and custom material properties. Laminates from the vendors are only available in limited thicknesses and dielectric properties. However, any layer thickness can be realized with AM. The dielectric constant and loss tangent can be lowered by selecting a low infill ratio, which also results in a lightweight structure. Besides, traditional fabrication methods such as photolithography require many fabrication steps and platforms. Monolithic fabrication with AM simplifies the fabrication process and cost. AM can also be used to fabricate over conformal platforms, while it is not possible with conventional fabrication techniques.

The following section explains and compares various additive manufacturing techniques used for realizing antennas and antenna arrays. A literature review of antennas using additive manufacturing is discussed in Section 1.2. Section 1.3 details the motivation and research focus of this dissertation. The contributions of this dissertation are listed in Section 1.4.

1.1   Additive Manufacturing Techniques

The best suitable technique for the fabrication of an antenna can be decided based on material selection, shape, and precision requirements. SLA, binder jetting, selective laser sintering (SLS) and selective laser melting (SLM) are the best techniques for realizing antennas with complex geometries, while inkjet printing, aerosol jet printing, fused deposition modeling (FDM) and micro-dispensing are suitable for multilayer antennas.

SLA builds the structure layer by layer with a photochemical process, forming polymers from photopolymer resin with UV laser. SLA is an inexpensive high precision technique and can be used to realize arbitrary shapes. It also provides smooth surface finish, which is important for high frequency antennas. However, it requires additional fabrication steps such as copper coating for metallization. In addition, SLA is not suitable for multilayer antennas. It is not possible to integrate with other AM techniques on a single platform as the structure is built inside a vat filled with photopolymer resin. Binder jetting uses binders to selectively bind the powder to build the structure. The powder can be metal, polymer, or ceramic for binder jetting. Selective laser sintering (SLS) and selective laser melting (SLM) are other AM techniques using powder. SLS and SLM use laser to sinter/melt the powder together. Material of SLS is polymer powder, while metal powder is used for SLM. Binder jetting, SLS and SLM can be used to achieve high precision and complex geometries. However, it results in a rough surface finish and generally requires post-processing such as electroplating to achieve smooth surfaces. These techniques are also not suitable for integration with other AM techniques and multilayer structures for the same reasons mentioned for SLA.

For multilayer structures, inkjet and aerosol jet printing can be utilized. Both techniques are multimaterial and use dielectric and metallic inks (such as silver nanoparticle inks - also known as SNP). Although, dielectric inks have significantly higher losses compared to thermoplastic polymers used by FDM. Layer thickness with these techniques are typically less than 10 μm. Thick substrates require many passes and curing/drying in between certain number of passes, therefore not practical. Host substrates such as liquid crystal polymer (LCP) or printed substrates with FDM are used for thick dielectric substrates. These techniques provide small feature size and they are

2

suitable for high frequency applications. FDM is the process of extruding heated thermoplastic filament through a nozzle to build the object layer by layer. It is a very inexpensive method compared to other AM techniques. It allows realizing thin to thick layers. Dielectric properties of the printed substrates can be modified by simply changing the infill ratio of the layers. This technique is also suitable for integration with other AM techniques. However, the surface profile is rough and wavy/bumpy due to under/over extrusion of filaments, and feature size is limited by the nozzle diameter. Microdispensing can be used to realize dielectric and metallic patterns on a surface. Material selection is not as limited as inkjet/aerosol jet printing as inks or pastes with high viscosity can also be printed with this technique. Micro-dispensing can be easily integrated with other AM techniques such as FDM. However, precision mostly depends on the nozzle diameter. Conductivity at higher frequencies can also be a problem as the printed lines have tapered edges.

Direct digital manufacturing (DDM) is an additive manufacturing (AM, three-dimensional (3D) printing) technique that builds an object layer-by-layer based on 3D geometry model. The object is realized from a CAD file and does not require significant human interaction or special tools such as masks. The whole process is performed on a single platform in one process. Therefore, there is not additional post-processing on another platform, which increases the fabrication time and complexity. It can combine multiple AM techniques such as FDM for dielectric layers and micro-dispensing for metallization to realize multilayer structures. In addition, micro-machining methods such as laser or micro-milling can be integrated for high precision and high frequency techniques. Laser micro-machining can provide higher conductivity by printing wider lines then cutting the edges [2]. This turns the low-density tapered edges to very dense high conductivity sharp edges where the current is concentrated at high frequencies. It can also be used to achieve small less than 100 μm gaps. DDM offers design flexibilities for multilayer devices such as custom thicknesses, shapes, and material properties. In addition to these, it can be used for packaging or embedding of MMIC/ICs and integrated with pick and place machines for a fully automated process.

3

1.2 Additively Manufactured Antennas

Additively manufactured antennas can be divided into two main categories, which are antennas with complex geometries (or 3-D antennas) and multilayer antennas. 3-D antennas are mostly made of a single material. They are either directly manufactured from metal or fabricated as polymer then plated for metallization. Multilayer antennas are formed of dielectric and metal layers. DDM or hybrid methods can be used to realize these antennas. Hybrid methods are a combination of AM and traditional fabrication techniques. Traditional methods are mostly utilized for metallization to achieve higher conductivity than AM provides.

1.2.1 Antennas with Complex Geometries

3-D antennas with complex geometries can provide better antenna performance such as wider bandwidth or narrower bandwidth. However, these shapes are complex, costly, and not practical with conventional fabrication methods. Recently, it has been shown that they can be easily and cost-effectively fabricated with AM, which opens new design flexibilities for 3-D antennas. References [3,4] demonstrate 3-D fractal antennas realized with AM. Before AM, these antennas are not practical with traditional methods, therefore, most of the work in literature lacks experimental verification of these antennas and are limited to design and simulation. [3] proposes a 3-D Sierpinski fractal monopole antenna. While fractal antenna provides wider bandwidth, it is also significantly lighter than non-fractal antenna since it uses only 25% volume of the non-fractal design. The antenna was fabricated using metal binder jetting since it provides higher precision and more mechanical strength compared to other AM techniques such as SLA. After the binder jetting process, the antenna was electroplated with copper to reduce the surface roughness. Reference [4] presents a comparison of different AM techniques for the realization of a 3-D Hilbert fractal antenna. SLA, SLS, and binder jetting were compared in terms of mechanical and electromagnetic properties. SLA and plating provided the best surface finish, therefore conductivity. SLS results in better conductivity compared to binder jetting, while both techniques are limited to frequencies below 30 GHz.

4

1.2.2 Multilayer Antennas

Multilayer antennas can be examined in two categories, which are antennas using hybrid techniques and antennas using DDM. Hybrid techniques are commonly utilized to achieve high conductivity. One approach is to use additional fabrication techniques for metallization. [5] demonstrates a 7.5 GHz patch antenna, which combines FDM for the antenna substrate and ultrasonically embedded metal mesh wire for metallization. By using embedding copper meshes inside the printed substrate, [5] achieves 5.5 dBi realized gain and 84% radiation efficiency without using high temperature that can deform the printed thermoplastic filaments. [6] proposes a 6.4 GHz tunable patch antenna using SLA for antenna substrate and damascene process for metallization. First, the antenna substrate with trenches is built with SLA. Metallization is achieved by sputtering titanium, copper, and removal of the unwanted metallization with sanding. While this technique allows embedding chips inside the structure and customization, it adds many post-processing steps and fabrication platforms which could cause fabrication errors due to misalignment. The inability of forming metallization on nonplanar or conformal surfaces is another disadvantage of using post-processing techniques. Another hybrid technique is to use a host substrate that can withstand high curing/drying temperatures of conductive pastes and inks. [7] uses inkjet printing to realize a 24.5 GHz Yagi-Uda antenna. SU-8 is used for the dielectric layer of the microstrip-to-slotline transition. Each dielectric layer has 5 μm thickness and after each pass the ink should be UV-cured. Building a thick substrate with this process would take a significant amount of time and SU-8 has a loss tangent of 0.04. Therefore, an LCP laminate from Rogers Corp. is used as a host substrate. For conductor layers, sintering is performed in addition to drying. As a result, 3 and 5 director Yagi-Uda antennas have 6 and 8 dBi maximum realized gain, respectively.

Other than using post-processing for metallization or utilizing host substrates, DDM can be used to realize multilayer antennas. [8] shows the 6 GHz half-wave dipole antenna volumetrically embedded into the dielectric structure. It uses FDM of ABS for dielectric layers and micro-dispensing of CB028 for metallization. The GCPW balun feed of the antenna is printed on an inclined surface. This design reduces the proximity of the feed network to the ground plane, which

reduces surface wave losses and results in a compact size. Reference [9] demonstrates a 2.6 GHz half-wavelength dipole antenna on artificial magnetic conducting (AMC). The substrates have low infill ratios, which reduces the dielectric constant. The antenna is realized by FDM of PC for dielectrics and micro-dispensing of silver ink for metallization. [10] also shows a 2.4 GHz inkjet printed patch antenna using a low infill substrate. 15% higher radiation efficiency was achieved by using a low infill antenna substrate.

1.2.3 Antenna Arrays

Additive manufacturing can be used to realize antenna arrays. [11] demonstrates a circularly polarized Ku-band 8×8 corporate-fed waveguide antenna arrays by metal and plastic AM. Mechanical and electrical properties of CNC milling, direct metal laser sintering (DMLS) and SLA are compared. DMLS provides high accuracy at the joints with monolithic fabrication which may be significant for high frequency applications. [12] also shows an antenna array using DMLS. The X-band horn antenna and patch antenna arrays are perforated to reduce the weight of the structure without significantly affecting the antenna performance.

Investigation of additively manufactured phased array antennas is relatively unexplored. There are only two phased arrays using AM in the literature. [13] demonstrates a polymer-based Ku-band 4-element steerable waveguide antenna array. Polyjet printing, FDM and electroplating are utilized for the array fabrication. [13] demonstrates the unit-cell of the first multilayer phased array antenna using DDM, which has seven metal layers and seven substrate layers. FDM of ABS is used for dielectric layers, while micro-dispensing of CB028 is used for metallization. While the phased array antenna demonstrates the capabilities of AM, it operates at lower microwave frequencies.

1.3 Motivation and Research Focus

The goal of this dissertation is to realize antennas and phased arrays with structural electronics. Multilayer antennas and phased antenna arrays using DDM are mostly demonstrated at

lower microwave frequencies (below X-band). High frequency antenna fabrication requires high precision in terms of dimensions and alignment. At or above X-band, the additively manufactured multilayer antennas in literature are using hybrid fabrication (partially printed). In addition, the antennas are not packaged with control electronics. Integration of electronics at higher microwave frequencies remains to be a challenge due to smaller unit cell sizes. The efficiency of the multilayer antennas and transmission lines should also be investigated and improved for higher frequencies due to high conductive and dielectric losses compared to standard PCB fabrication. Effective RF conductivity of conductive pastes is lower at higher microwave frequencies due to trapezoidal cross sections and surface roughness.

To address these needs in the literature, this dissertation demonstrates X/Ku-band multilayer wideband antennas and cavity-backed phased antenna array unit cells with embedded active MMICs by harnessing design flexibilities offered by DDM. In order to minimize feed network losses and increase radiation efficiency, losses of planar transmission lines are minimized using additive manufacturing and micromachining techniques.

1.4 Contributions

Previously, a Ku-band aperture-coupled single patch antenna with low-infill antenna substrate [14] is presented. In [15], this antenna is extended to a dual-polarized stacked patch antenna with polarization switch. However, this design is not suitable for 2D array applications since unit cell size is larger than half wavelength at the center frequency. In addition, the bandwidth of the antenna does not cover the entire Ku-band. Chapter 2 demonstrates a Ku-band dual-polarized patch antenna with embedded MMIC switch using DDM. The antenna bandwidth covers the entire Ku-band while providing high cross-polarization levels and isolation. MMIC switch is embedded within the feed substrate and connected to feed lines through 3D interconnects. 3D interconnect approach provides high return loss and smaller packaging. In order to minimize feed network losses, microstrip line substrate designs are optimized by adjusting infill ratio and substrate thickness. In addition, antenna feed design allows selecting optimum FDM directions for each feed line

to minimize surface roughness losses. The presented Ku-band antenna consists of 13 alternating dielectric and conductive layers realized with a single DDM platform and offers state-of-the-art performance.

To allow platform installations and reduce back-lobe radiation of the aperture-coupled patch antenna, we demonstrated an X-band cavity-backed wideband aperture-patch antenna with and without the phase shifter using DDM. The antenna element is designed for phased array applications. Therefore, an MMIC phase shifter is fully embedded into the substrate for half-wavelength spacing. The phased array unit cell design, fabrication and experimental verification are discussed in Chapter 3.

Higher frequency planar phased array antennas using additive manufacturing remain unexplored. A 2×2 sub-array with embedded control ICs is designed in Chapter 4. The phased array unit cell in Chapter 3 is used in the array design. Shift registers are added to reduce a large number of control and bias lines.

Conductor losses are significant additively manufactured printed transmission lines. Reference [2] uses laser micromachining on the edges of the coplanar waveguides to increase conductivity silver pastes at higher microwave frequencies. However, the effect of laser micromachining significantly depends on line geometry due to skin and edge effects. In Chapter 5, the effect of laser micromachining on microstrip lines and grounded coplanar waveguides is investigated for the first time. Effective conductivity and line attenuations are characterized up to 30 GHz.

Chapter 6 summarizes the accomplishments of this dissertation. Based on the investigations and observations in the dissertation, future work on the RF devices using additive manufacturing is also discussed.

Chapter 2: 3D Printed Wideband Multilayered Dual-Polarized Stacked Patch Antenna with Integrated MMIC Switch

2.1 Introduction

Additive manufacturing has been established as a fabrication technique for several end-use products and provides low-cost, lightweight, conformal solutions [1]. Compared to conventional fabrication methods, AM/DDM does not require many fabrication steps and introduces capabilities that are suitable to pursue innovative design solutions [16]. For RF applications, DDM enables multilayered RF electronics with customized material properties, thicknesses, shapes, metallization patterns and structural packaging.[1] The moderate dielectric losses ($\sim \tan\delta = 0.0075$) and conductivities ($\sim 10^6$ S/m) of materials employed in the DDM processes have motivated researches to pursue antenna and transmission line designs operating at frequencies ranging from low GHz to mm-wave bands. Recent literature has investigated DDM of antennas and demonstrated that fully printed multilayered antennas with high radiation efficiencies are achievable. These demonstrations are at frequencies below X-band. For example, reference [13] demonstrates the first known additively manufactured multilayer phased antenna array at 2.45 GHz by utilizing in-situ finite filament fabrication (FDM) of acrylonitrile butadiene styrene (ABS) filaments and microdispensing of CB028 silver conductive paste (aka DDM process), where microdispensing refers to high precision deposition of liquid materials. By using DDM and similar material combinations, reference [8] presents a 6 GHz half-wave dipole antenna volumetrically embedded into a dielectric structure. In [9], a multilayer low profile 2.6 GHz antenna utilizing FDM of polycarbonate (PC) and microdispensing of silver ink is presented. Reference [18] demonstrates the effect of infill percentage

---

change on permittivity and loss tangent of ABS fabricated with FDM. References [10, 19] also investigate low infill dielectrics for antenna substrates. On the other hand, antenna demonstrations with DDM operating at or above X-band are not reported. In these bands, antenna demonstrations of additive manufacturing are so-far limited to structures that are partially printed. This is achieved by using an additional fabrication step (such as copper cladding, spraying, etc.) for metallization over a dielectric part that is realized with the additive manufacturing technique. For instance, references [20, 21] present Ku and Ka-band horn antennas using stereolithography (SLA) of plastics and copper cladding. SLA is not suitable for multilayer antennas as material types are limited to liquid polymers and resin, cannot be used for metals. Selective laser sintering (SLS) provides wider material selection including metals. Reference [22] presents multilayer TLs and MIM capacitors with SLS; however, each layer requires coating/spraying the surface with dielectric/conductive inks and removing the unsintered material. Reference [7] employs a liquid crystalline polymer (LCP) laminate as the host substrate for dielectric and metallic ink layers. While some of the fabrication methods (SLA and metal coating, SLS) are not suitable for multilayer antennas such as microstrip antennas and embedded applications, others (inkjet printing, aerosol jet printing) commonly require a support material as they are not practical for thick substrates.

The major goal of this chapter is to utilize design flexibilies of DDM for realizing a fully printed dual-polarized antenna with radiation efficiency and return loss performances exceeding 80% and 10 dB, respectively, across the Ku-band (12-18 GHz). The antenna should operate with excellent polarization purity and more than 25 dB isolation between feed ports. In addition, the antenna must be suitable to be employed as a unit cell within a half-wavelength spaced phased antenna array. Based on the literature review outlined above, meeting these performance metrics implies a significant advancement over the recently reported antennas realized with additive manufacturing. To address the wide bandwidth and dual-polarization needs, an aperture stacked patch antenna fed with microstrip lines is selected for the design. As shown in [14], for antennas operating at lower frequency bands, the antenna substrates are formed from low-infill ratio ABS and their thicknesses are customized to maximize radiation efficiency and bandwidth. However, in contrast to existing

literature, this dissertation also investigates the geometry of the microstrip feed lines for the first to time to further maximize the radiation efficiency and minimize losses in potential phased array implementations. This is achieved through a detailed investigation of substrate thickness, infill ratio, and infill direction. As such, this dissertation achieves the lowest attenuation (0.25 dB/cm) at 18 GHz with respect to the microstrip lines reported in recent works. Polarization purity is achieved by resorting to the well-known dual-offset feed line excitation through crossed apertures. For improved polarization purity and isolation, the dual-offset microstrip feed lines belonging to the different polarization excitations are located on separate sides of the ground plane. The MMIC switch package (PQFN) is embedded within the structure to make connections with these feed lines using a ramped 3D interconnect approach. Thanks to its shorter line lengths, this interconnect approach is shown for the first time to support a higher return loss (30 dB vs 20 dB) and loss performance over a traditional via based interconnect. The packaging approach also enables the antenna to be utilized within a half-wavelength spaced array. Additional dielectric/conductor layers can be added to the antenna structure to include a MMIC phase shifter package as well, however, the extension to an operational beam-steering phased array is beyond the scope of this article. The fabricated antenna consists of a total of thirteen dielectric and conductive layers. As desired, a 45% $|S_{11}|$<-10 dB impedance bandwidth is achieved across the entire Ku band (12-18 GHz) with >80% radiation efficiency. The dissertation is organized as follows: Section 2.2 presents the investigation of substrate thickness, infill ratio and infill direction to minimize the loss of the microstrip feed lines utilized in the antenna structure. Section 2.3 details the antenna design and 3D printed interconnect performance utilized for MMIC polarization switch inclusion. Experimental verification of the antenna integrated with the MMIC switch is presented in Section 2.4. Suitability of the antenna element in terms of size and feed line losses for phased array development is demonstrated in Section 2.3. Concluding remarks are provided in Section 2.5.

2.2 Microstrip Line Characterization for Minimizing Feed Line Losses

2.2.1 Substrate Stack-up

Figure 2.1 shows the substrate stack-up of the microstrip lines that are utilized for the antenna feed. ABS, a well-known thermoplastic polymer, is utilized as the dielectric material. The substrate is built up by melting the ABS filament and depositing layer by layer on the printer platform. The goal is to investigate if flexibilities available through the slicing software (i.e. independent control on infill ratio, layer thickness, and printing direction of each layer) can be optimized to minimize the insertion loss (IL) of the microstrip lines. Among these design flexibilities, infill ratio has already been a heavily investigated design parameter for enhancing antenna performance or achieving control over transmission and reflection properties [23, 24]. Infill ratio refers to the thermoplastic content inside the volume. Naturally, low infill ratio substrates exhibit lower dielectric constants and loss tangents due to the higher air content within the volume. Therefore, minimization of microstrip line loss can be achieved through the utilization of low infill ratio substrates. However, as the following section will demonstrate, it is also equally important to consider the line geometry in terms of overall substrate thickness and printing direction to achieve the best possible performance – factors that have not been demonstrated to date to our knowledge. Based on this reasoning, we investigate microstrip lines constructed from ABS with infill ratio down to 25%. In printing studies, we could not go below 25% infill ratio while maintaining a good print quality in terms of surface roughness and uniformity. It is also important to note that microdispensing conductive paste over low infill ratio materials is impossible due to paste leakage into the structure. Hence, substrate layers with infill ratios of 100% are necessary under the conductors. In the printing process, it is possible to make trade-offs between the nozzle size of the printing tip and overall printing time. However, thicker layers that can be printed with large nozzle sizes tend to exhibit larger surface roughness. It is already known from other transmission line geometries such as strip lines that losses due to conductors increase significantly with surface roughness at higher frequencies [25]. Due to these reasons, 100% infill ratio layers that are directly under the microstrip conductor are
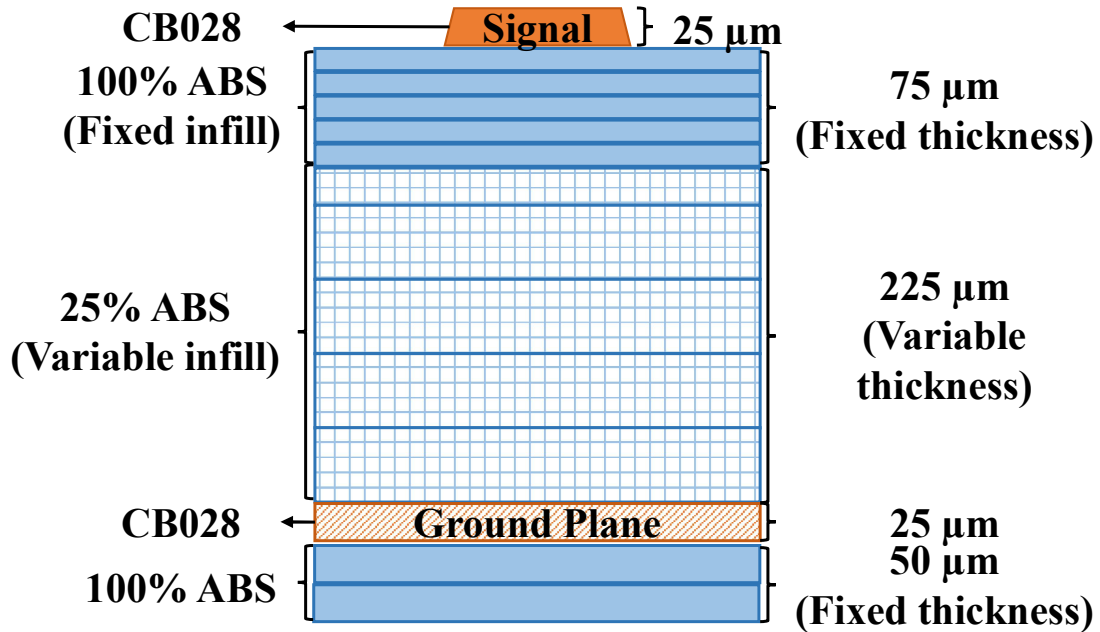
Figure 2.1: Substrate stack-up of the DDM microstrip line.

printed using the minimum available thickness of 15 μm. The total thickness of the 100% infill ratio substrate under the microstrip conductor is taken as 75 μm (i.e. 5 × 15 μm) since no significant improvement in surface roughness is observed beyond this thickness. In this substrate stack-up, the overall thickness of the 25% infill ratio substrate does not seem to affect the surface roughness of the 100% infill substrate that is directly under the microstrip line conductor. This allows forming the 25% infill ratio substrate in thicker layers to achieve faster printing speed. For the substrate stack-up, the majority of the 25% infill ratio substrate is therefore formed with printing of 50 μm thick ABS layers. The ground plane is microdispensed over a 50 μm thick 100% ABS substrate. Microdispensing refers to deposition of liquid materials with high control over the volume less than 100 picolitres by adjusting printing speed, pressure, and valve opening. Microdispensing of CB028, a silver nanoparticle paste from DuPont, is the technique used in this dissertation to form the conductive traces.

2.2.2 Design

Thermoplastic materials have lower loss tangent compared to dielectric inks such as SU-8 (ε_r=2.85 and tanδ=0.04) [26]. However, losses are still higher than standard materials such as hydrocarbon or PTFE ceramic composites and this increased loss challenging for high frequency DDM devices. For high frequency antenna arrays, feed network losses degrade the RF performance, and heating caused by these losses restricts the power handling capabilities. These are the main motivators for investigating the design flexibilities of the DDM process as a whole, not only infill ratio as in [10, 19], but also in geometry and printing directions.

The dielectric properties of the ABS can vary with supplier, color, and frequency [18]. Therefore, before proceeding with microstrip line designs, ABS filament available in our lab has been characterized for dielectric constant and loss tangent values by printing $0.4 \times 3 \times 6$ cm^3 sheets and using a Damaskos 125HC thin sheet tester. Figure 2.2 depicts the measurements within the 4.3 GHz to 17 GHz band. Since frequency dependency of dielectric constant and loss tangent is not significant by being less than 0.1% over this band. Figure 2.2 presents the averaged values of the material properties. ABS with 25% infill ratio exhibits a dielectric constant and loss tangent of 1.28 and 0.0027, respectively. As expected, it exhibits the lowest loss tangent justifying the choice of this infill ratio ABS for forming the majority of the microstrip line substrate. On the other hand, ABS with 100% infill ratio exhibits dielectric constant and loss tangent of 2.39 and 0.0075, respectively.

Following the characterization of the ABS material properties, we proceed with the design of the microstrip line geometry. As stated, unlike conventional fabrication methods, DDM allows controlling substrate thickness on demand. This opens the possibility of utilizing the best substrate thickness for lowest microstrip line losses. In general, conductor loss decreases with increasing substrate thickness while radiation loss increases. To investigate this, insertion losses of 10 mm long 50 Ω microstrip lines for different substrate thicknesses and infill ratios are simulated using Ansys HFSS. To achieve 50 Ω characteristic impedance for the microstrip line over the substrate stack-up, line width is parametrically swept to achieve a return loss value exceeding 30 dB. In these

simulations, conductivity of CB028 silver paste is taken as 1.65 MS/m [14]. Figure 2.3 shows the attenuation of these microstrip lines per unit length at 18 GHz – the highest frequency of interest for the antenna designs presented in the following sections. As expected, microstrip lines realized with 25% infill ratio ABS performs the best while at very thin and thick substrates attenuation becomes almost equal with the lines realized over 50% infill ratio substrates due to the dominance of conductive and radiation losses, respectively. It should be noted that microstrip lines are wider on low infill ratio substrates in order to maintain identical 50 Ω characteristic impedance. Microstrip line loss with the 25% infill ratio substrate remains relatively flat within the range of 300 to 400 μm substrate thicknesses, demonstrating the importance of utilizing the best thickness for minimizing losses. To reduce radiation losses that may occur at line discontinuities, we selected the substrate thickness as 300 μm to implement the microstrip feed lines in the presented antenna realizations. Specifically, the lowest simulated loss at 18 GHz is 0.25 dB/cm and offers 0.11 dB/cm improvement over the best achievable performance with the 100% infill substrate design.Replacing the CB028 conductivity with copper's conductivity of 58 MS/m in the simulation model shows that the loss at 18 GHz comes down to 0.08 dB/cm from 0.25 dB/cm. Due to this reason, increasing conductivity of 3D printed pastes/inks continues to be an active research area [2, 27].

Another factor that affects the microstrip line attenuation at high frequency is the alignment between the microdispensed microstrip line and infill direction of the top layer (the direction of the 100% infill ratio ABS filaments deposited to form the top layer that is directly under the signal line as depicted in Figure 2.1). The edge roughness of the microstrip line due to this misalignment may introduce additional conductive losses. Reference [28] has demonstrated that surface roughness dependent on the infill direction varies the ohmic losses of microstrip lines at microwave frequencies up to 5 GHz. As frequency increases, it is expected that the current on the microstrip line will be more concentrated in the line edges and therefore the effect of edge roughness will be even more pronounced. Our work in [14, 15] demonstrates this issue through microstrip line characterizations, however, microstrip lines were realized from 100% infill ratio substrates without substrate thickness vs. attenuation considerations. This dissertation demonstrates this
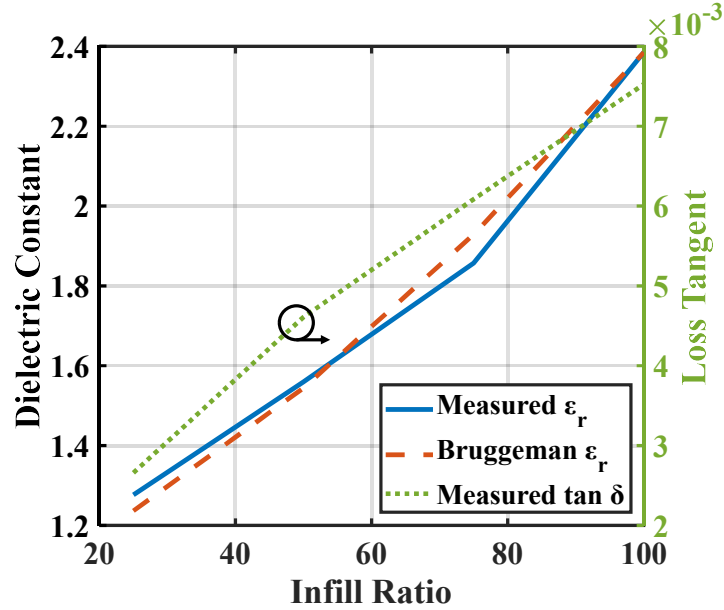
Figure 2.2: Measured dielectric constant and loss tangent for ABS exhibiting different infill ratios.

effect experimentally with microstrip lines that utilize the 25% infill ratio substrate and optimized substrate thicknesses. Specifically, parallel and perpendicular ABS deposition directions with respect to the microstrip line direction are characterized as shown in Figure 2.4. Based on these characterizations, the antenna design (discussed in Section 5.3) utilizes controlled infill directions within its structure to realize the best possible radiation efficiency performance by keeping feed line losses at minimal.

2.2.3 Fabrication

High frequency device fabrication requires further precision as the effect of surface roughness and dimensional variations are more pronounced than at lower frequencies. The surface of substrates fabricated by FDM have waviness due to under-extrusion of the filaments, and this topographical variation degrades the effective RF conductivity of traces deposited on top of them. Reference [29] states that fine-tuning of the extrusion multiplier can achieve smooth surfaces while avoiding over extrusion. 0.97 is found to be the best extrusion multiplier in terms of minimizing surface roughness with the Slic3r as slicing software. By incorporating alternating layer thicknesses

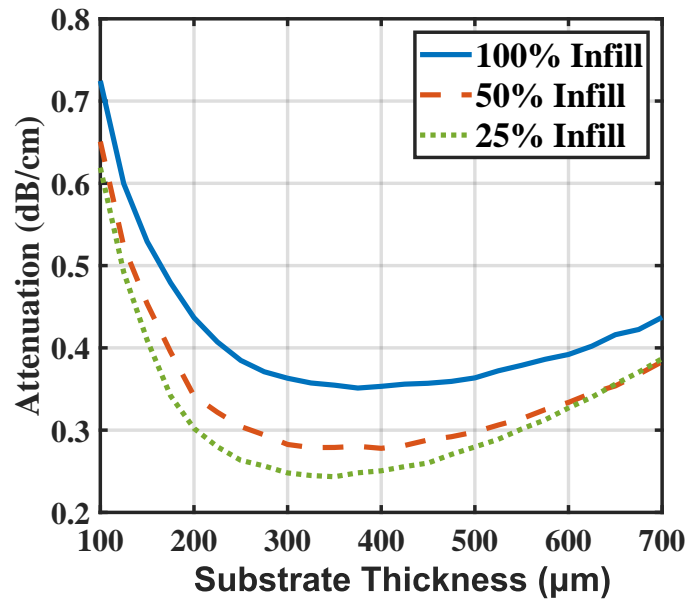Figure 2.3: Attenuation of microstrip lines for different substrate thicknesses and infill ratios at 18 GHz.
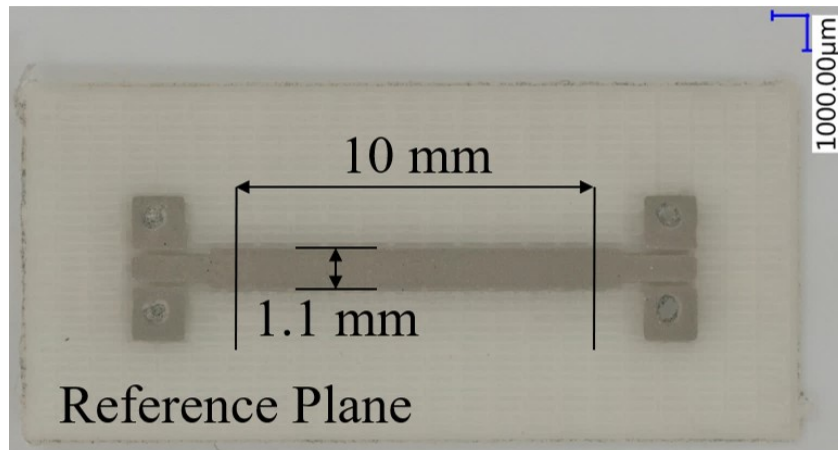

Figure 2.4: Microscope image of the printed microstrip line.

and fine-tuning the extrusion multiplier, 3 μm peak-to-valley height is achieved within reasonable printing time. All presented devices are printed using an nScrypt 3Dn-Tabletop system including both FDM for dielectric materials and micro-dispensing for metallization. Dimensional variations due to microdispensing are minimized by decreasing single pass line width and printing speed. For instance, sharper corners are achieved with slower speeds. For a certain line width, air pressure and printing speed are adjusted. Specifically, 100 μm wide single pass lines are microdispensed with 3 psi air pressure at 5 mm/s.

Multilayer structures necessitate good adhesion between silver paste and thermoplastic layers. First, a slurry of ABS and acetone is applied to the surface of the 90°C heated printer bed to improve adhesion to the bed. This eliminates the edge warping of ABS for thick structures. The slurry is also applied on the CB028 layers prior to ABS deposition to improve adhesion. CB028 layers are dried at 90°C bed temperature for an hour before ABS deposition. A high nozzle temperature (240°C) for melting the filament is also used for good adhesion.

2.2.4 Characterization

Microstrip lines are formed with 10 mm total length with parallel (0°) and perpendicular (90°) FDM orientation choices with respect to the line elongation. Figure 2.4 shows the microscope images of the printed microstrip line and reference planes. Figure 2.5 shows the microscope images of tilted microstrip lines belonging to parallel and perpendicular FDM orientations. A Keysight N5227A PNA Microwave Network Analyzer and Cascade Microtech probe station are used for taking S-parameter measurements up to 20 GHz. The line excitations are performed with 650 μm pitch ground-signal-ground (GSG) probes. Probe effects are removed from the measurements by utilizing thru-reflect-line (TRL) calibration kits that are designed and printed on the identical substrate stack-up. Figure 2.6 depicts the $|S_{21}|$ performance of the microstrip line samples. It clearly shows that FDM orientation with respect to the line length is an important factor for minimizing the attenuation even though the line geometry in terms of substrate thickness and infill ratio is designed to attain the best performance. Specifically, at the highest end of the Ku-band (i.e. 18 GHz), the
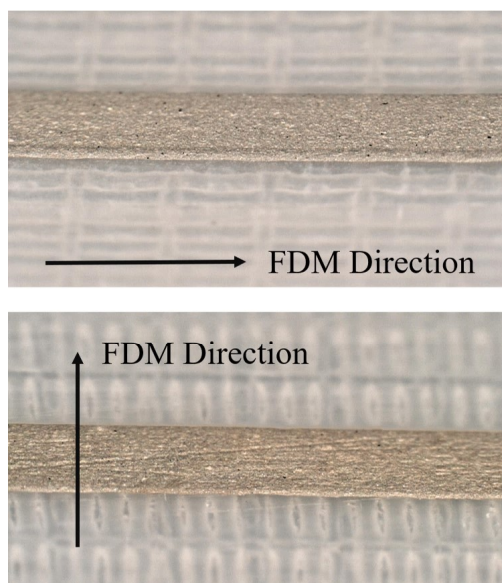
Figure 2.5: Close-up microscope image of the tilted microstrip line.

loss of the microstrip line increases by 0.08 dB/cm. An RF circuit simulator can be employed to show that such increase in attenuation implies a 60% decrease in the effective RF conductivity. On the other hand, parallel FDM direction with respect to the microstrip line provides the lowest attenuation. Curve fitting as shown in Figure 2.6 demonstrates that the measured $|S_{21}|$ performance corresponds to that of a microstrip line exhibiting an effective conductivity of 1.75 MS/m at Ku-band. It is important to note that all characterized microstrip lines exhibit $|S_{11}|$<-25 dB, implying a good impedance match with 50 Ω as they are designed.

Table 2.1 compares the attenuation of the fully printed microstrip lines reported in this dissertation with data reported in the literature. Microstrip lines fabricated by inkjet and aerosol jet printing of dielectric and silver inks have been characterized in [30, 31] with losses around 2.8-6 dB/cm at 20 GHz. These jet printed microstrip lines demonstrate significantly higher attenuation due to high loss tangent of the dielectric inks utilized in the printing process. References [32, 33] demonstrate loss improvements with suspended microstrip line geometries that employ air substrates. Although [32] demonstrates a slightly lower attenuation than the microstrip lines reported in this work, the suspended line approach requires more than one printing platform and is
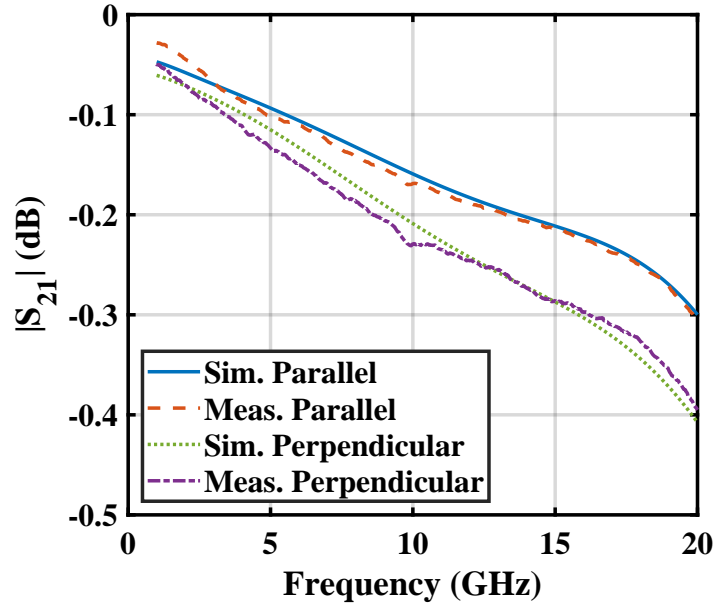
19

Figure 2.6: Measured and simulated $|S_{21}|$ (dB) of 10 mm long microstrip line with parallel and perpendicular FDM directions.

less practical for implementing multilayered antennas, arrays, and feed networks. Microstrip lines realized over 100% infill ratio ABS have been reported to perform with 0.19 dB/cm and 0.52 dB/cm attenuation at 3 and 18 GHz, respectively [13, 14]. The microstrip line losses reported in this work is 0.07 dB/cm and 0.25 dB/cm at 3 and 18 GHz, respectively. At 18 GHz, this is a 0.27 dB/cm reduction in loss and constitutes the minimum attenuation reported in the literature for microstrip lines that are fully printed using a single manufacturing platform.

2.3 Dual-polarized Stacked Patch Antenna

Having established the microstrip line geometry for the antenna feed network, we proceed with the design of the dual-polarized stacked patch antenna to meet the goals indicated in the introduction section i.e. impedance matching bandwidth across entire Ku-band, compact footprint enabling extension into antenna arrays, dual-polarization and polarization selection capability. Achieving a good cross-polarization level and meeting the compact footprint requirement while employing a cost effective commercial-off-the-shelf SPDT PQFN switch package (MACOM

Table 2.1: Attenuation of transmission lines using additive manufacturing.

Reference	Loss (dB/cm)	Fabrication Technique	Properties
[13]	0.19 at 3 GHz	DDM	Microstrip, ABS, CB028
[31]	6 at 20 GHz	Inkjet	Microstrip, SU-8, Silver ink
[30]	2.8 at 20 GHz	Aerosol jet	Stripline, Polyimide, Silver ink
[32]	0.09 at 5 GHz	SLA, micro-dispensing	Suspended microstrip, SLA resin, CB028
[33]	0.17 at 4 GHz	Polyjet	Microstrip, VeroWhitePlus, Ti/Cu
[14]	0.55 at 18 GHz	DDM	Microstrip, ABS, CB028
This work	0.17 at 10 GHz; 0.25 at 18 GHz	DDM	Microstrip, ABS, CB028

MASW-008322 DC-20 GHz SPDT) necessitates embedding the switch within the antenna structure. Structural embedding of active and control components is generally costly and challenging with multilayered PCB technology. On the other hand, DDM may provide a cost effective approach to realize such embedded RF electronics. The design of the presented antenna with the embedded polarization selection switch is carried out in two major steps to be able to focus on individual performance aspects: 1) Substrate stack-up and antenna design to maximize antenna performance without considering the switch packaging (Section 3.1 and 3.2); 2) Switch packaging (Section 3.3). Experimental verification is provided in Section 3.4.

2.3.1 Substrate Stack-up

Figure 2.7 shows the substrate stack-up of the antenna. Dashed arrows show the direction of FDM. Figure 2.8 shows the two dimensional view of the feed layout. All dimensions are in millimeters. Switch integration is shown in Figure 2.11. To achieve a low level of cross-polarization (<-15 dB), dual offset feed lines are utilized over the crossed coupling apertures. Placement of the feed lines on different sides of the coupling aperture further minimizes the feed line asymmetry within the vicinity of the coupling apertures. Our recent work in [14] already demonstrated an aperture coupled single patch antenna, which can provide 25% impedance matching bandwidth within the Ku-band when implemented with low infill ratio ABS substrate. An attempt was made to

provide dual polarization capability to this earlier antenna by resorting to a square patch geometry. However, inclusion of the crossed coupling apertures and square patch geometry caused a bandwidth reduction that could not be alleviated by adjusting the antenna substrate thickness. Consequently, the antenna was redesigned with the substrate stack-up shown in Figure 2.7 to exhibit a stacked patch geometry to provide further bandwidth enhancement. The feed substrate thicknesses are selected as 0.3 mm based on the microstrip line loss studies presented in previous section. Antenna manufacturing is performed from top to bottom starting with the printing of a 200 μm-thick 100% ABS layer and microdispensing of the upper square patch. 25% infill ratio ABS substrates with varying thicknesses are utilized as the antenna substrates. The microstrip feed line at the bottom of the stack-up i.e. first feed line in Figure 2.7 remains exposed to facilitate the attachment of an edge connector for experiments. First feed line is on the same layer of RF signal input to the SPDT switch. Its substrate stack-up is based on section 5.2.1 since it may be used to implement long RF feed lines in a full antenna array implementation. The second feed line is embedded within the structure. Due to the layer printing sequence, the substrate of second line is printed after microdispensing of the line conductor. This minimizes the loss by reducing the substrate material under the line. Therefore, a triangular prism-shaped void (200 μm wide and 225 μm deep) is created under the 100 Ω lines. The line widths of 2nd feed line are designed within the full substrate stack-up by performing two-port S-parameter analysis of 10 mm long lines and minimizing the return losses. The antenna has 8 dielectric and 5 conductor layers.

2.3.2   Antenna Design

First, a single-polarized center-fed aperture coupled single square patch antenna is designed to operate at 15 GHz similar to the antenna presented in [14]. The dimension of this antenna element is 6 x 6 mm^2 and agrees with half guided wavelength ($\lambda_g/2$) size expectation on a 25% infill ABS substrate. Antenna substrate thickness of this design is relatively thick at 2 mm (i.e. $\sim \lambda_0/10$, λ_0 denotes the free space wavelength at 15 GHz) and it does not meet the impedance bandwidth criteria. Consequently, substrate stack-up was expanded to be like in Figure 2.7 to accommodate
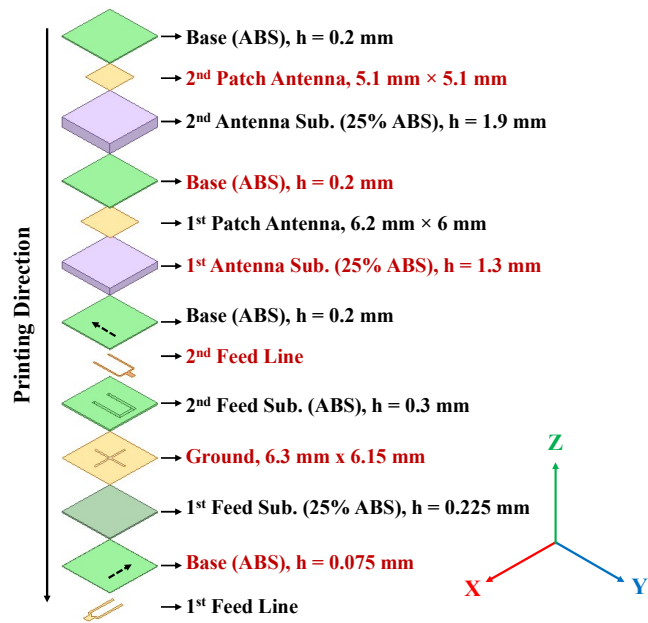
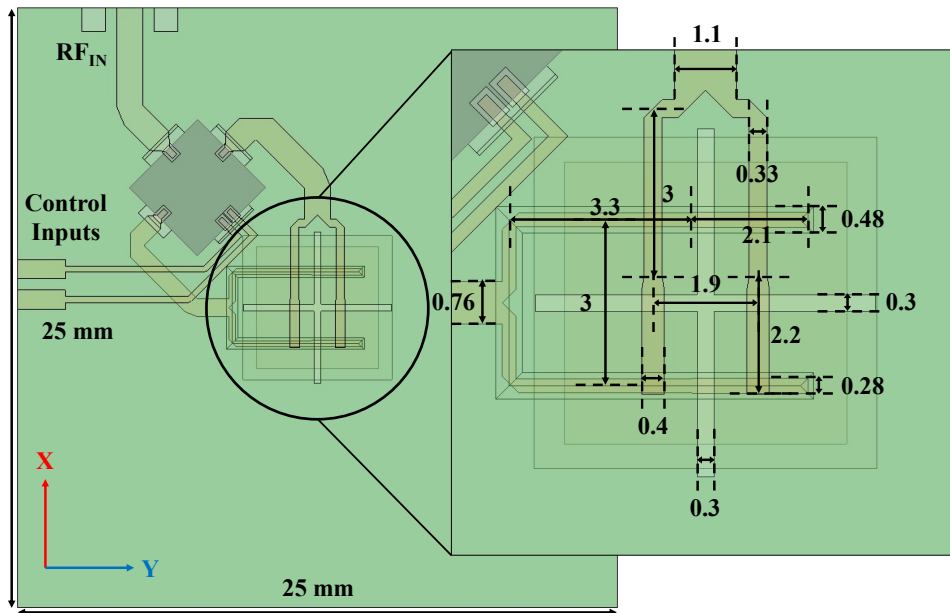Figure 2.7: Substrate stack-up under the antenna.

Figure 2.8: 2D view of the antenna feed layout.

a second square patch element. The second patch element and its substrate are initially taken to be identical with the first patch. In this step, the antenna is still single-polarized but substrate for second feed layer is introduced into the design without accommodating a feed line. For this stacked aperture-patch geometry and initial dimensions, the design approach reported in [34] is followed to achieve the desired performance goals. Specifically, mutual coupling between the two patches and mutual coupling between the aperture and first patch generate two S11 loci in the Smith Chart. Patch sizes relative to each other and the substrate thickness of the second patch affect the coupling between the patches and can be used to control the size of the higher frequency locus. Aperture size and the thickness of the first patch affect the location of the low frequency locus. Studying these parameters along with the feed line stub length results in 45% $|S_{21}|$<-10 dB bandwidth to cover the Ku-band (12-18 GHz). After the completion of the design for single-polarized case, the antenna geometry is modified to incorporate dual offset feed lines and a crossed slot aperture to provide dual-polarization capability. Dual-offset feed lines are selected for their low level of cross-polarization performance [35, 36]. Second feed substrate is also slightly modified to include air groove under the 100 Ω lines to minimize their ohmic losses. The distance between the 100 Ω lines are adjusted with parametric sweeps to achieve desired coupling between the slot and lower patch (i.e. low frequency locus size). The stub lengths of the feed lines are parametrically adjusted to move the impedance loci to the center of the Smith Chart. To improve the impedance matching performance of the second feed line, the length of the first patch along the second feed line is also slightly increased.

Figure 2.9 presents the simulated $|S_{11}|$, $|S_{22}|$, and $|S_{21}|$ performance of the antenna with feed lines extended to the switch. It is observed that, for both polarizations, the antenna operates with more than 45% $|S_{11}|$<-10 dB bandwidth around 15 GHz center frequency. The bandwidth of the antenna covers the entire Ku-band. The isolation between the polarization feed lines is larger than 28 dB. Figure 2.10 presents the simulated broadside-realized gain as a function of frequency for both polarizations. Realized gain attains a peak value of 8.6 dBi and 8.4 dBi at 15 GHz.
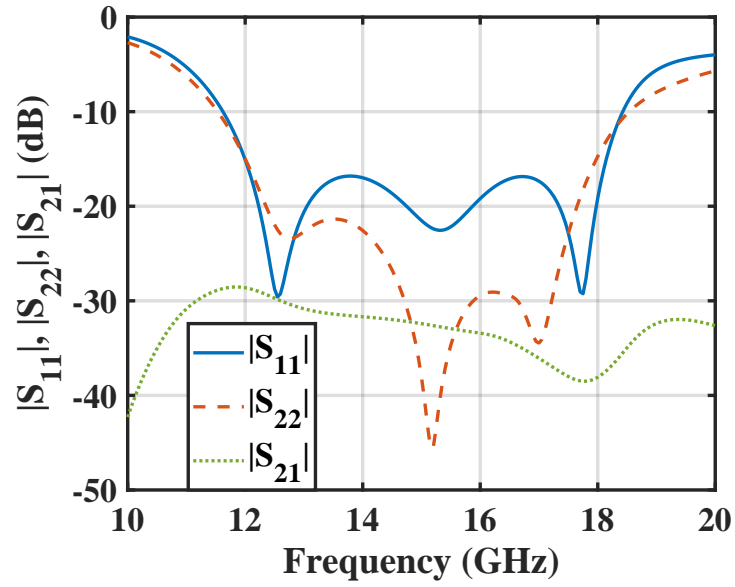
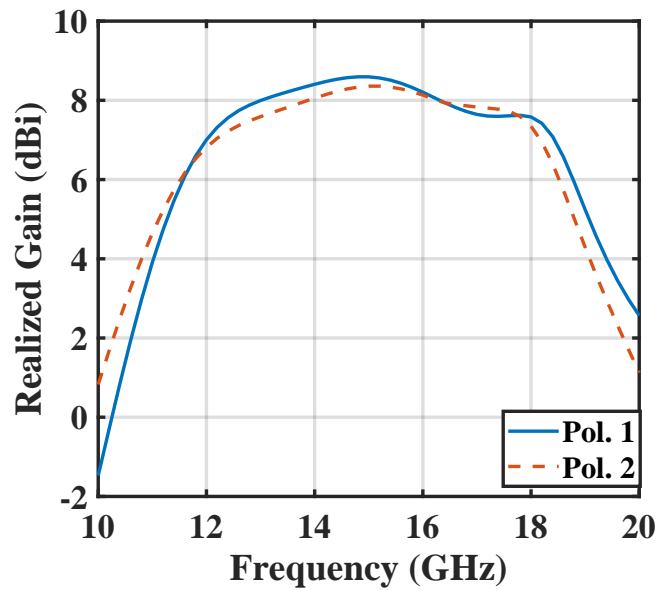Figure 2.9: Simulated reflection coefficients of polarization 1 and 2 and $|S_{21}|$ (dB).

Figure 2.10: Simulated realized gain of the dual-polarized aperture-stacked patch antenna without the switch for both polarizations.

Realized gain is larger than 6.8 dBi across the impedance matching bandwidth. Simulated radiation efficiency is 87% and 81% at 15 GHz.

2.3.3 Switch Integration

A MACOM MASW-008322 DC-20 GHz SPDT switch in PQFN package (4 mm × 4 mm) is used to select the polarization due to its high isolation performance. According to the datasheet, the switch has more than 40 dB isolation up to 20 GHz, and this is higher than the isolation between antenna feed lines. Figure 2.11 shows the substrate stack-up around the switch from 3D and 2D perspectives. The PQFN switch package directly lands on the ground plane for minimizing the length of the cross-layer electrical connections for the feed lines. This eliminates the need for vias that would run from the bottom of the PQFN package to the ground plane. The PQFN switch package is also placed close to the antenna element to obtain a total footprint of 9 mm x 9.5 mm. The RF and control pads of the package are isolated from the ground plane by introducing 0.125 mm gap between the conductive traces. The RF lines are taken to the feed layers #1 and #2 through a ramped transition as illustrated in Figure 2.12. All dimensions in Figure 2.12 are in millimeters. The geometry of the ramped transitions is parametrically adjusted to achieve a high return loss levels. Since feed line #1 and #2 are different (embedded within the stack-up vs. exposed), the transition geometries are slightly different from each other. The transition geometry for the input RF signal line is identical with Feed line #1 since both microstrip lines are on the same layer of the substrate stack-up. As shown in Figure 2.13, the return loss is greater than 40 dB for exposed transition and greater than 33 dB for the embedded microstrip line transition. Insertion losses of the transitions are less than 0.12 dB. The transition geometry for the input RF signal line is identical with Feed line #1 since both microstrip lines are on the same layer of the substrate stack-up.

As stated, the overall footprint size including the SPDT switch makes the antenna element suitable for 2-D array applications. Although a complete phased array manufacturing is beyond the scope of this article, in Figure 2.14 we present a potential layout/model for a 4 x 4 phased array that can harness the designed antenna element. In this model, the antenna elements are excited with
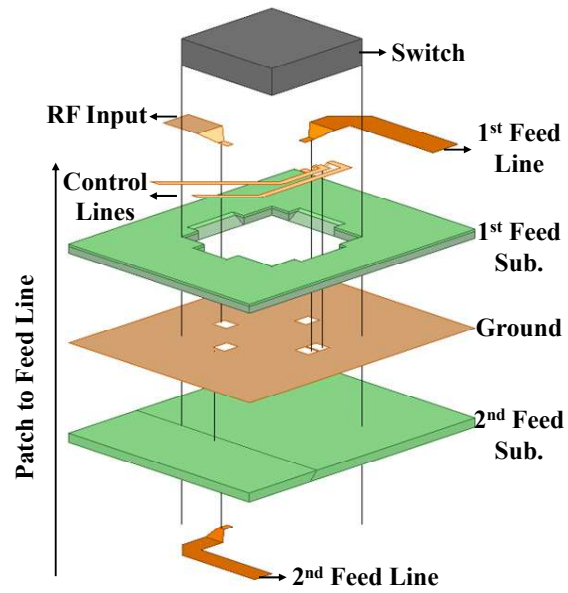
26

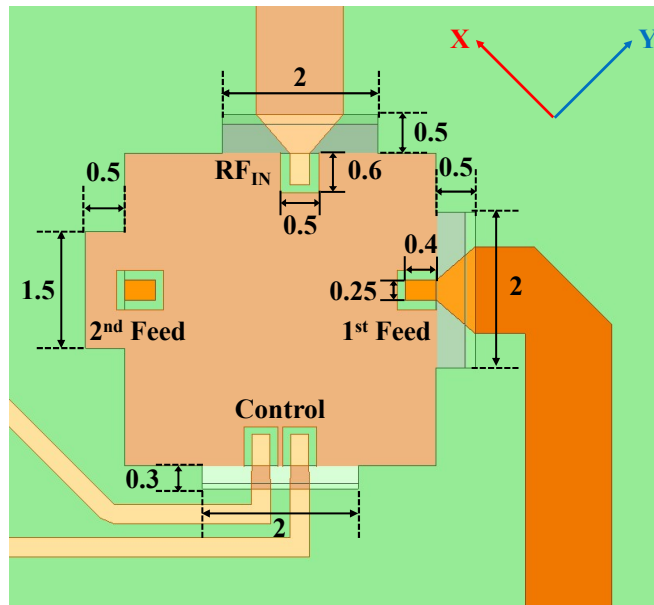Figure 2.11: Expanded view of the switch integration.

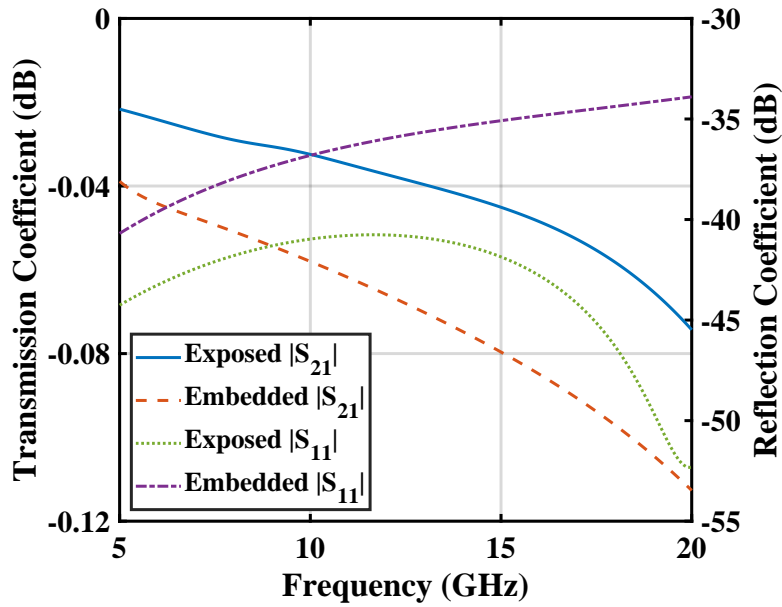Figure 2.12: Top view of the switch integration.

Figure 2.13: Simulated S-parameters of the interconnects.

lumped ports placed at the switch outputs. In a practical realization, the signal routing for the array can be carried out in a separate layer by transitioning the RFIN signal line from each switch. The design of the RF signal routing should be carried out according to the guidelines (i.e., line width, layer thickness, FDM direction, FDM infill ratio) described in Section 2 of this dissertation for feed loss minimization. Figure 2.15 depicts the simulated impedance matching of antenna elements #1, #2 and #3. As seen, all elements are well matching. Simulated mutual coupling among the antenna elements is below 12.4 dB, while the highest coupling occurs between second feed line of antenna elements #2 and #3. Simulated broadside realized gain of the array is 16.5 dBi for polarization 1 and 15.6 dBi for polarization 2, implying 83% and 76% radiation efficiency. Realized broadside gain is expected to be almost identical between the x and y-polarizations due to the customization of printing directions and line geometries to minimize the feed losses. The half power beam width (HPBW) of the array for polarization 1 is 22.4°in the E-plane and 24.7°in the H- plane. The HPBW of the array for polarization 2 is 22.1°in the E-plane and 24.8°in the H-plane.
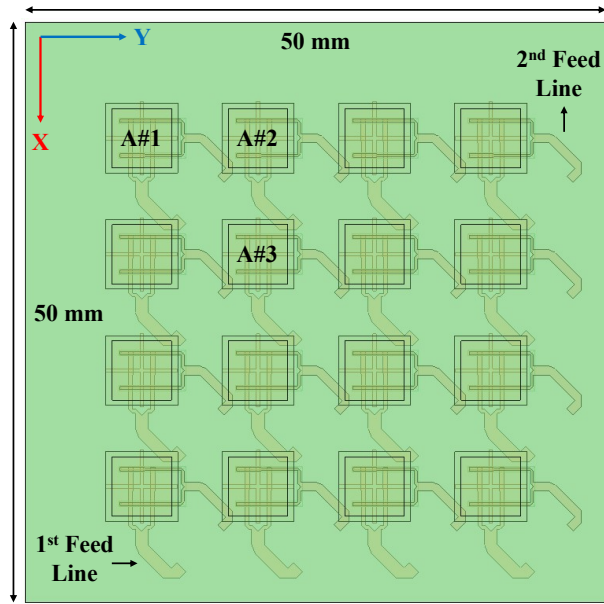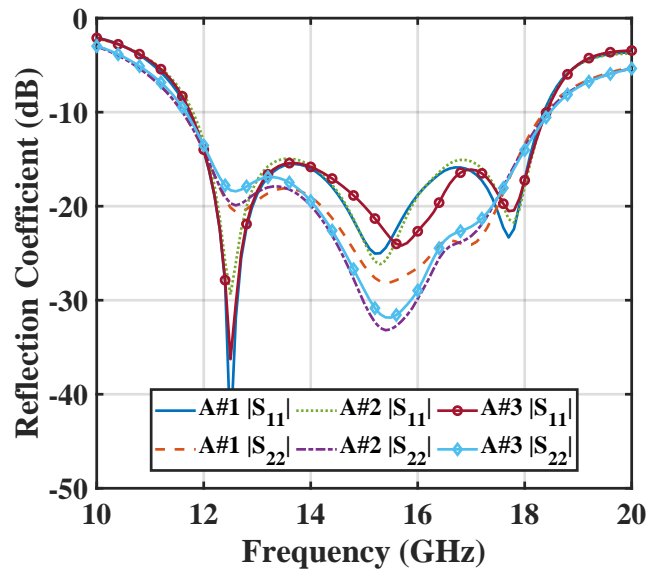
Figure 2.14: Top view of the 4 x 4 antenna array.

Figure 2.15: Simulated reflection coefficient of the antenna elements #1, #2 and #3.

2.3.4   Experimental Verification

Figure 2.16 shows the fabricated antenna with SMA connector, socket, and switch. All dimensions shown are in millimeters. Since the switch is not fully embedded within the structure like in [37], a small droplet of cyanoacrylate glue is used at the corners of the switch package to prevent it from moving. Likewise, the SMA connector and socket packages are mounted to the edge of the substrate using glue instead of screws. Electrical connection from switch pads, SMA connector pin, SMA connector ground, and socket pins to the microdispensed pads/lines are made with H20E (a conductive silver epoxy from EPO-TEK). The assembly is kept in oven at 80°C for 3 hours to cure the H20E. Return loss of the antenna is measured from 10 to 18 GHz using a Keysight E5063A network analyzer. Figure 2.17 shows the comparison of measured reflection coefficient of the dual-polarized patch antenna for different switch states. The antenna return loss is greater than 10 dB between 10.8 GHz-18 GHz for polarization 1, and 11.1 GHz-18 GHz for polarization 2; whereas, predicted bandwidth is 45% around 15 GHz. The bandwidth of the antenna element covers the entire Ku-band as expected. There is a good agreement between the simulated and measured results considering that simulated $|S_{11}|$ and $|S_{22}|$ in Figure 2.9 do not include the effect of the switch, connector launch and connector.

Figure 2.18 presents the simulated and measured realized gain versus frequency and validates the wideband performance. For realized gain simulations, RF_{IN} and feed line are connected with a mitered bend for each polarization. Switch loss as a function of frequency obtained from manufacturer is subtracted from the simulated realized gain along with 0.4 dB connector loss. When mounted in a 50 Ω transmission line system, the switch exhibits ̃1 dB insertion loss at 10 GHz with excellent impedance matching and isolation characteristics (see data sheet for typical frequency dependent characteristics). Simulated realized gain is 6.8 dBi for polarization 1 and 6.4 dBi for polarization 2 at 15 GHz. There is a good agreement between the realized gain results for both polarizations being within 0.7 dB of each other.

Figure 2.19, Figure 2.20, Figure 2.21, Figure 2.22 show the simulated and measured normalized radiation patterns of the antenna element at 15 GHz. Front-to-back radiation ratio for
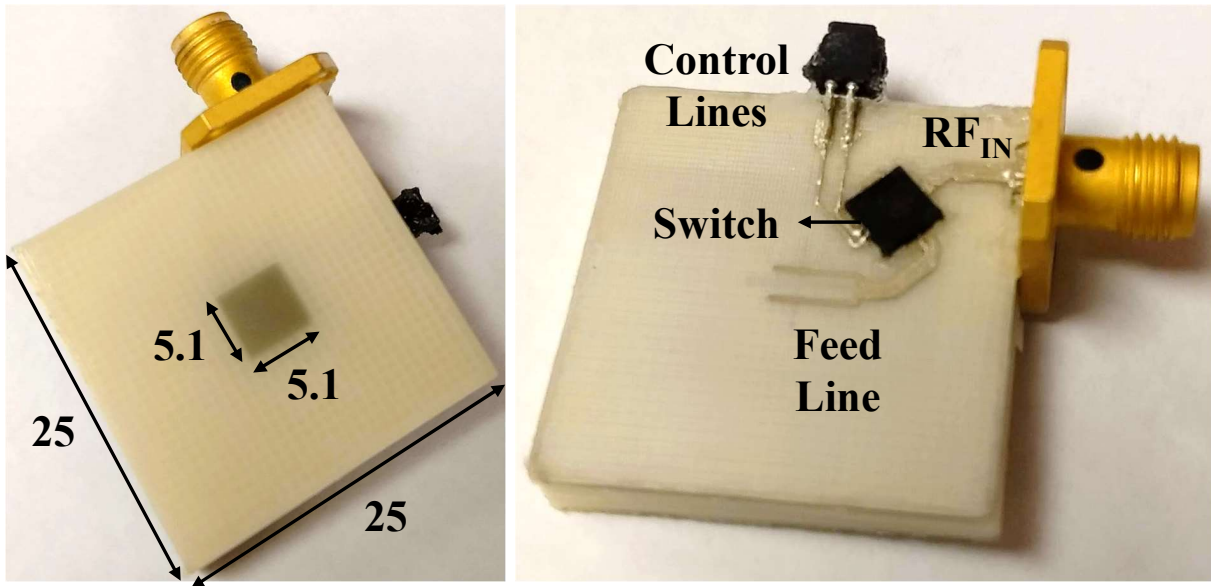
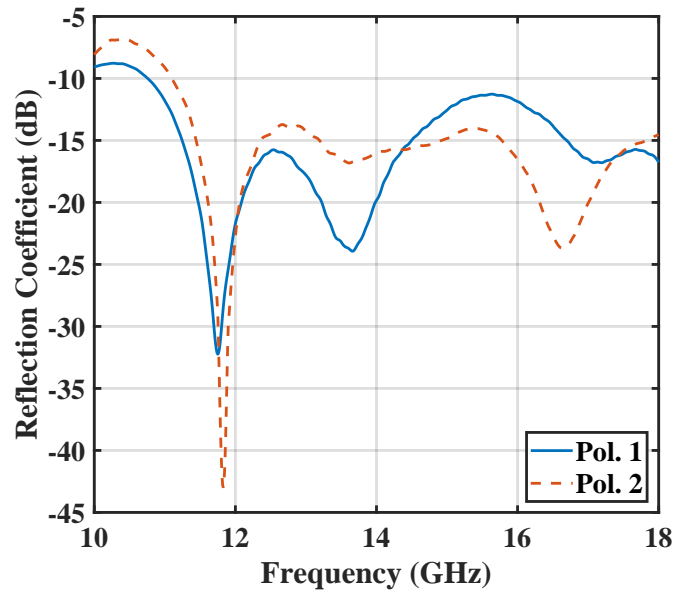Figure 2.16: Top and bottom view of the fabricated antenna.

Figure 2.17: Measured reflection coefficient (dB) of the dual-polarized antenna for both polarizations.
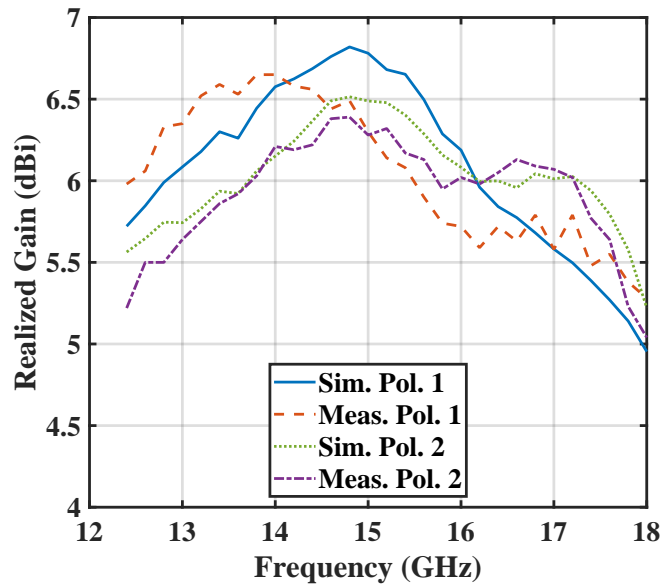
Figure 2.18: Measured reflection coefficient (dB) of the dual-polarized antenna for both polarizations.

polarization 1 is 18.7 dB for the E-plane and 16.3 dB for the H-plane. For polarization 2, front-to-back ratios of the E-plane and the H-plane are 15.6 dB and 14.9 dB, respectively. Aperture radiation contributes to this front-to-back ratio. However, as demonstrated in reference [37], substrate stack-up can be further expanded by using DDM capabilities to incorporate an embedded cavity for minimizing the back radiation. Cross-polarization gain is lower than the co-polarization gain by 18.7-18.9 dB for the E-plane and 20.2-23.3 dB for the H-plane. Due to the agreement between the simulation and measurement data in radiation patterns and peak realized gains, radiation efficiencies for polarization 1 and 2 can be estimated to be close to the simulated 87% and 81% values.

Table 2.2 provides a comparison between the antenna presented in this dissertation and additively manufactured antennas available in literature. References [6,19,33] demonstrate a hybrid manufacturing approach to realize patch antennas. This approach employs additive manufacturing for antenna substrates, and a damascene process or copper tape for metallization, which require multiple platforms. Reference [10] demonstrates a high radiation efficiency fully inkjet-printed patch antenna utilizing a low infill antenna substrate. However, this work is realized at lower

Figure 2.19: Simulated and measured polarization 1 E-plane co-polarization and cross-polarization normalized radiation patterns of antenna.

Figure 2.20: Simulated and measured polarization 1 H-plane co-polarization and cross-polarization normalized radiation patterns of antenna.
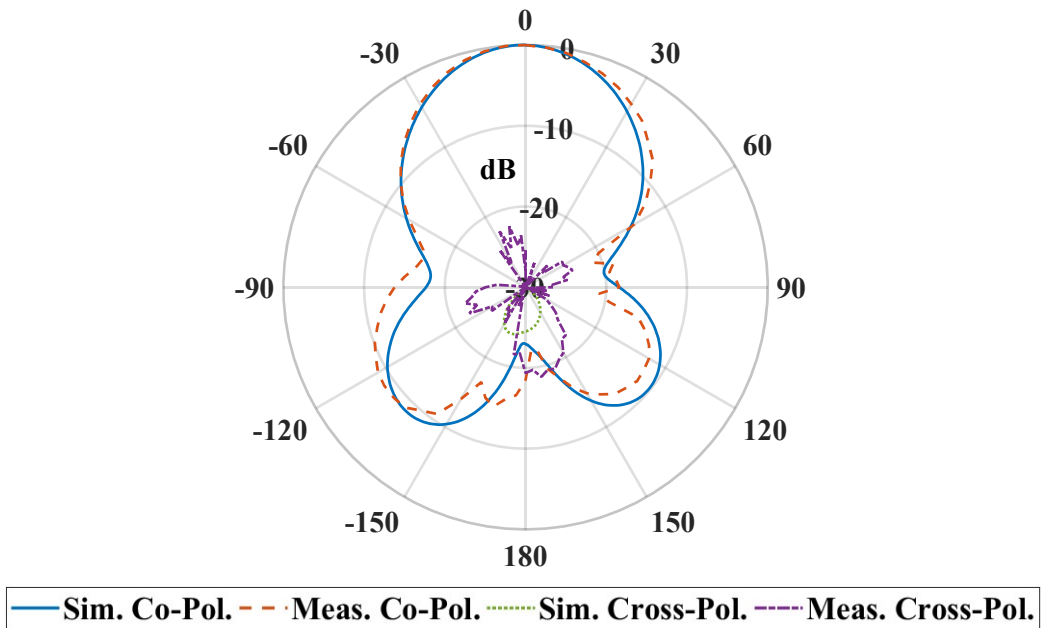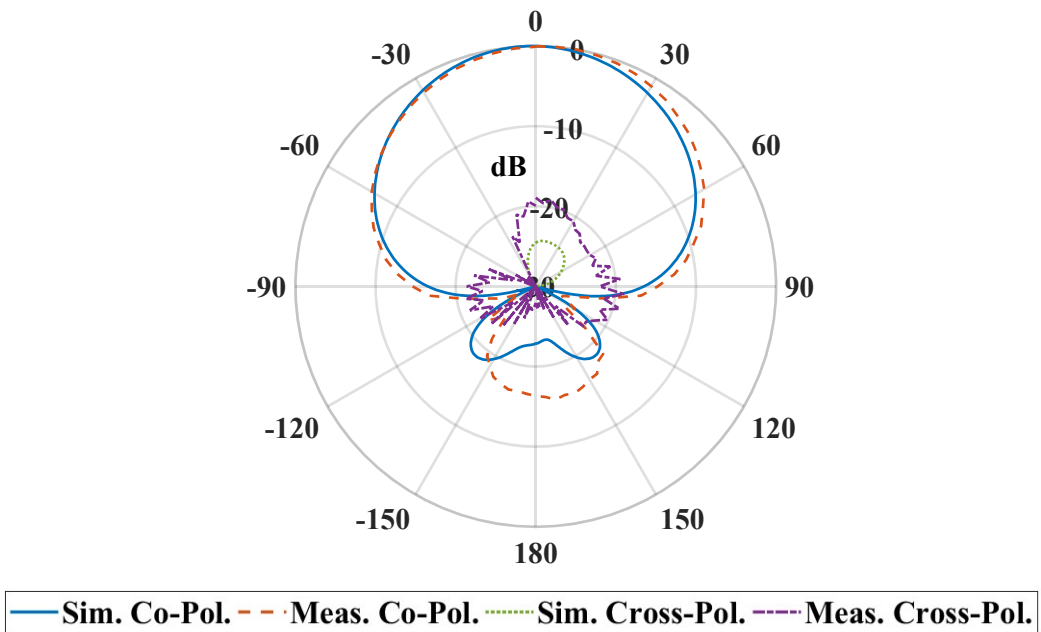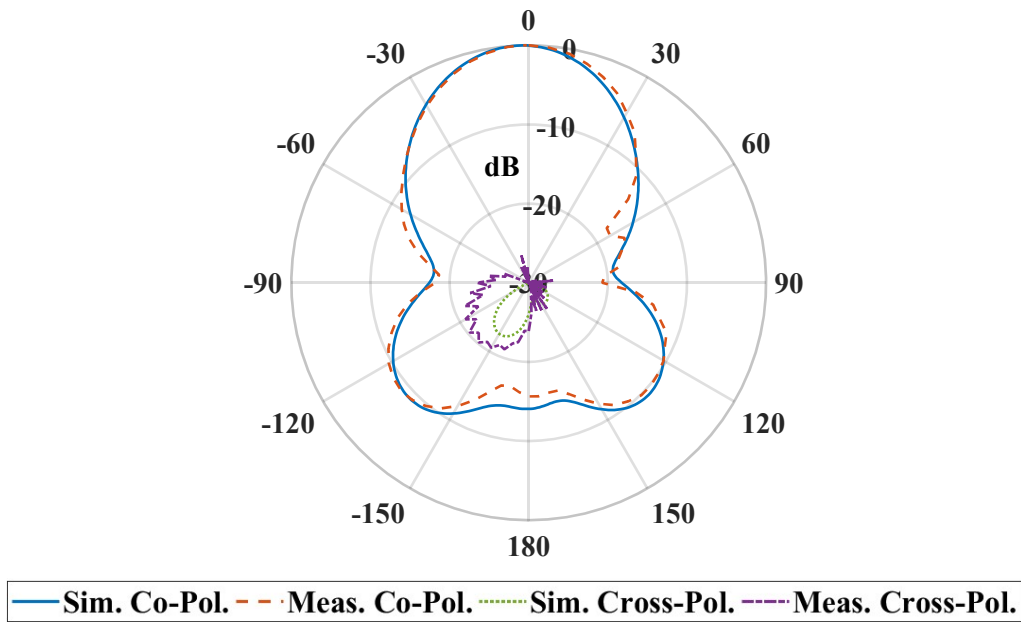
Figure 2.21: Simulated and measured polarization 2 E-plane co-polarization and cross-polarization normalized radiation patterns of antenna.
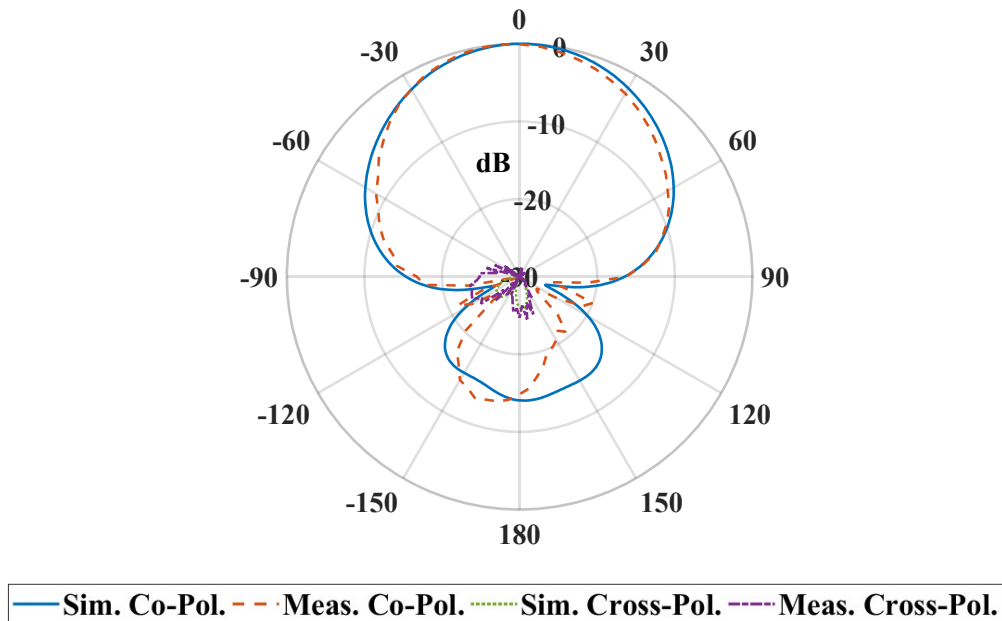

Figure 2.22: Simulated and measured polarization 2 H-plane co-polarization and cross-polarization normalized radiation patterns of antenna.

Table 2.2: Comparison of antennas using additive manufacturing.

Ref.	Freq. BW	Realized Gain Rad. Eff.	Fab. Techniques	Materials & Antenna Type
[33]	4.49 GHz 4.5%	7.25 dBi NA	Polyjet + Damascene	VeroWhitePlus, Ti/Cu Patch
[6]	6.4 GHz 5%	5.48 dBi NA	SLA + Damascene	Resin, Ti/Cu Patch
[10]	2.4 GHz 8%	8 dBi 81%	Inkjet	UV-Cured Polymer, Silver ink, Patch
[19]	2.33 GHz 6%	-3.8 dBi 18%	FDM	NinjaFlex, Copper Tape, Patch
[5]	3.58 GHz 7%	4 dBi NA	FDM + wire-mesh embedding	Polycarbonate, Copper, Patch
[38]	7.5 GHz 15%	5.5 dBi 84%	FDM + wire-mesh embedding	ABS, Copper, Patch
[9]	2.6 GHz 8%	NA	DDM	PC, Silver ink, Dipole over HIS
[13]	2.45 GHz 48%	-2.5 dBi NA	DDM	ABS, CB028, Dipole
This work	15 GHz 45%	6.3 dBi 81-87%	DDM	ABS, CB028, Stacked Patch, Dual Pol, Packaged IC

microwave frequencies, where dielectric and conductor losses are not significant. References [5,38] present 3D-printed patch antennas with high radiation efficiency. However, metallization using ultrasonic wire-embedding requires additional platforms, and thus is not practical for multilayer structures and chip integration. References [9, 13] demonstrate fully-printed dipole antennas on single platform using DDM. However, these antennas operate at lower microwave frequencies.

2.4 Concluding Remarks

A fully printed multilayer Ku-band aperture-patch antenna is presented. The antenna is fabricated with FDM of ABS and microdispensing of CB028. Custom substrate compositions are utilized to improve the bandwidth, gain and efficiency performance of the antenna. A dual-polarized stacked patch antenna is designed and experimentally characterized to exhibit 6.3 dBi realized gain at 15 GHz, >80% radiation efficiency, and operating with 45% $|S_{11}|$ <-10 dB bandwidth. Moreover,

the antenna is integrated with a SPDT switch to provide electronic polarization control. Microstrip lines with different geometry and material arrangements are also investigated to minimize line losses. Specifically, fully printed microstrip lines with 0.25 dB/cm measured insertion loss at 18 GHz are demonstrated. The line loss is better than those reported to date in literature. The presented studies shows that the fully printed Ku-band antennas and antenna arrays packaged with control RF electronics (such as switches and phase shifters) is feasible and promising to perform with high radiation efficiency and antenna performance by harnessing the design flexibilities of additive manufacturing.

Chapter 3: Phased Array Antenna Element with Embedded Cavity and MMIC Using Direct Digital Manufacturing

3.1 Introduction

DDM allows implementing compact, cost-effective, light-weight RF systems consisting of multiples of alternating dielectric and conductive layers.[2] DDM's design flexibilities in material choices, layer thicknesses, and material shapes can be harnessed to enhance the RF performance to the level of those implemented with traditional manufacturing. Typically, antennas manufactured with AM techniques such as stereolithography selective laser sintering are not suitable for multilayer structures. Inkjet and aerosol jet printing can be used for multilayer RF device fabrication with high precision. However, these techniques have limited material selection and high dielectric losses, and they cannot be integrated with other AM techniques [7]. In contrast to these AM techniques, DDM has moderate dielectric losses, achieves thicker parts, and it does not require a host substrate. In reference [14] and Chapter 2, we harnessed the design flexibilities of DDM to realize Ku-band antennas with wide bandwidth and high radiation efficiency. However, these antennas are not suitable for printing on planar/conformal platforms since they are printed from antenna to feed line. These anteannas also exhibit high back radiation due to radiating aperture. In order to reduce back-lobe radiation, a cavity is embedded and printing direction is reversed. This chapter presents the fabricated cavity backed antenna operating with 23.8% $|S_{11}|$ <-10 dB and 7.2 dBi realized gain. The front-to-back ratio of the antenna is greater than 20 dB. Recent work [39] has demonstrated that DDM process can be utilized to integrate monolithic microwave integrated circuit (MMIC)

components with low interconnect losses. This chapter presents the latest progress in this area by structurally integrating an MMIC package towards the realization of multilayer wideband phased array antenna element at X-band. The antenna utilizes four metallization and five dielectric layers with various infill ratios to operate with 23% impedance matching bandwidth and 81% radiation efficiency. Packaged MMIC phase shifter is embedded inside the structure through selective FDM and interconnected to the signal and control lines through microdispensing.

3.2 Wideband Cavity-backed Patch Antenna

3.2.1 Substrate Stack-up

Figure 3.1 shows the substrate stack-up of the cavity-backed antenna. The printing is performed from bottom layer to top layer in order to enable future applications over platforms. Printing starts with FDM of support layer consisting of 0.25 mm-thick 100% infill ABS. The dielectric constant of ABS is 2.4, and loss tangent is 0.006. Parametric studies are conducted to determine the smallest cavity height that does not affect the impedance matching. The cavity bottom, which is extended by 1 mm from the footprint of the sidewalls, is formed on the support substrate by microdispensing Novacentrix HPS-FG57B silver ink. The 1.5 mm long sidewalls of the cavity is realized inside two solid ABS layers with thickness of 1.25 mm and 0.25 mm. The 0.25 mm ABS layer acts as the microstrip feed line substrate. The sidewalls are formed as HPS-FG57B filled vias with 1.5 mm periodicity and 0.4 mm radius. The 50 Ω microstrip feed line is converted into a coplanar waveguide (CPW, 0.1 mm gap and 2 mm center conductor) at the edge of the substrate to facilitate an interface with the RF connector. After microdispensing feed line, antenna fabrication continues with FDM of 0.25 mm thick ABS layer that forms the microstrip feed line substrate. This substrate layer is slightly retracted around the edges by selective FDM of ABS to expose the CPW transition. Microdispensing of silver paste is performed over this substrate to form the ground plane hosting the coupling aperture. Microstrip line and CPW ground are connected through the walls of retracted feed substrate. Following the micro-dispensing of the ground plane, FDM of a 3 mm thick 50% infill ABS layer (ε_r = 1.6, tanδ = 0.003) is performed to
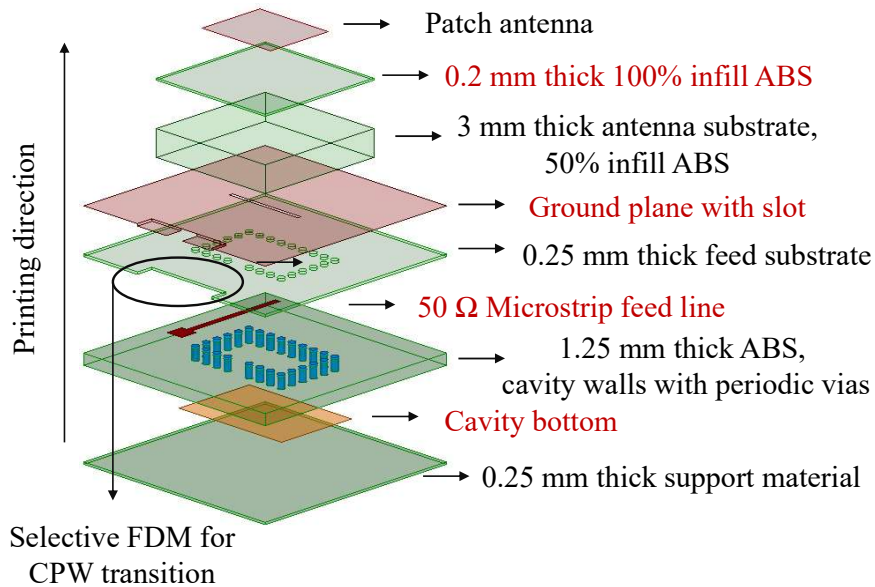
Figure 3.1: Substrate stack-up of the cavity-backed antenna.

realize the antenna substrate. The lower infill ratio and thickness of this substrate provides wide impedance bandwidth ($\sim$ 20%) and high radiation efficiency (>80%). FDM of a 0.2 mm thick solid ABS layer is performed over the low infill ratio substrate to enable micro-dispensing of the patch antenna without leakage issues. The lateral size of the antenna substrates are 15 × 15 mm^2 suitable for realizing traditional half-wavelength spacing. The bottom solid ABS substrates exhibit a lateral size of 25 × 25 mm^2. This enables to place the RF connector away from the antenna in stand-alone radiation characterizations. It is important to note that during the printing process, ABS surfaces are milled prior to micro-dispensing to minimize loss associated with surface roughness. Milling is an already incorporated functionality available within the nScrypt 3Dn-Tabletop system and performed as a part of the printing process. Overall, the antenna consists of four conductive layers and five dielectric layers with customized infill ratios and selective FDM. Figure 3.2 shows the photo of the fabricated antenna with a SMA connector attached for characterization.
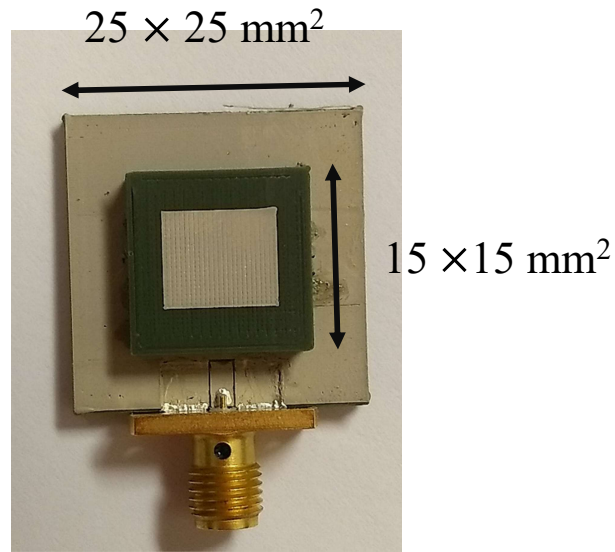
Figure 3.2: Fabricated cavity-backed antenna.

3.2.2 Experimental Verification

The cavity-backed antenna is fabricated and tested. Figure 3.3 shows the simulated and measured $|S_{11}|$ (dB) of the antenna. The antenna has 23.8% measured $|S_{11}| < -10$ dB bandwidth. Simulated $|S_{11}| < -10$ dB bandwidth of the antenna is 18.7%. There is a good agreement with the measured performance. The differences are due to the microstrip-to-CPW transition. Figure 3.4 shows the simulated and measured broadside realized gain of the antenna. The antenna exhibits 7.2 dBi peak gain at 10.4 GHz. It has more than 6 dBi realized gain between 9-11 GHz.Figure 3.5 shows the simulated radiation pattern of the antenna for E-plane and H-plane at the center frequency. Simulated front-to-back ratio is greater than 20 dB. Figure 3.6 shows the measured H-plane radiation pattern of the antenna at 10 GHz. The antenna exhibits more than 20 dB front-to-back ratio. The simulated radiation efficiency is 81% for the model including the extended feed line and CPW line transition. This also confidently represents the radiation efficiency of the fabricated antenna based on gain comparison as the simulated and measured patterns are perfectly aligned with identical realized gains.
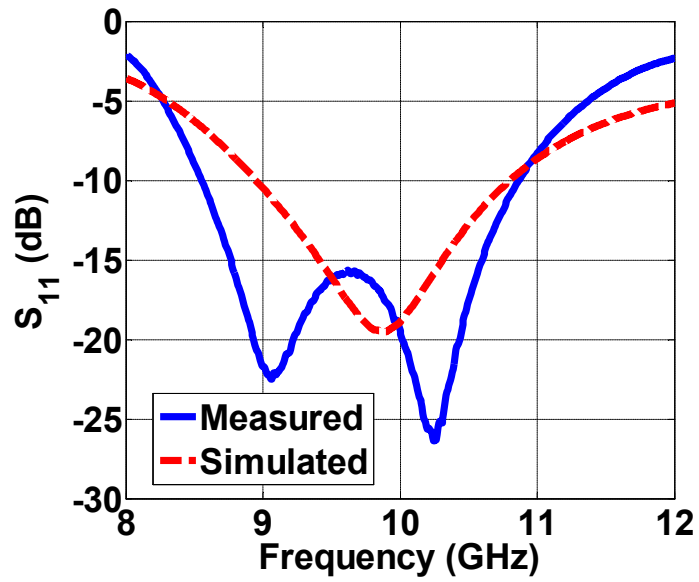
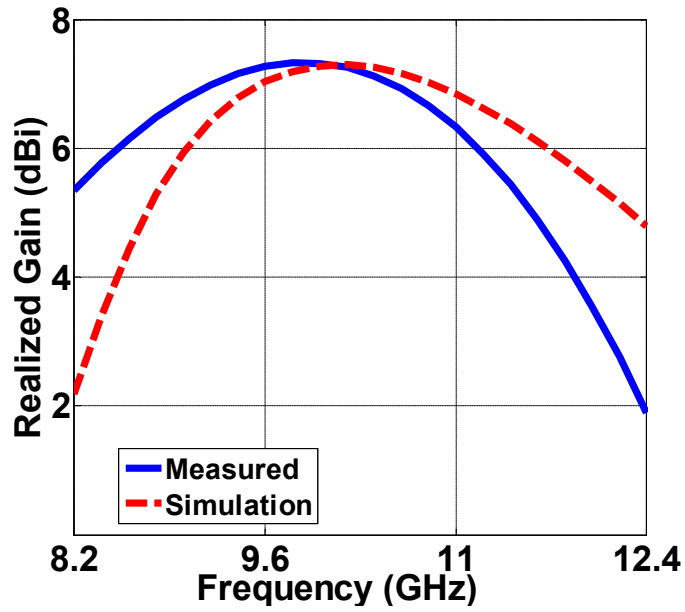Figure 3.3: Reflection coefficient of the cavity-backed antenna.

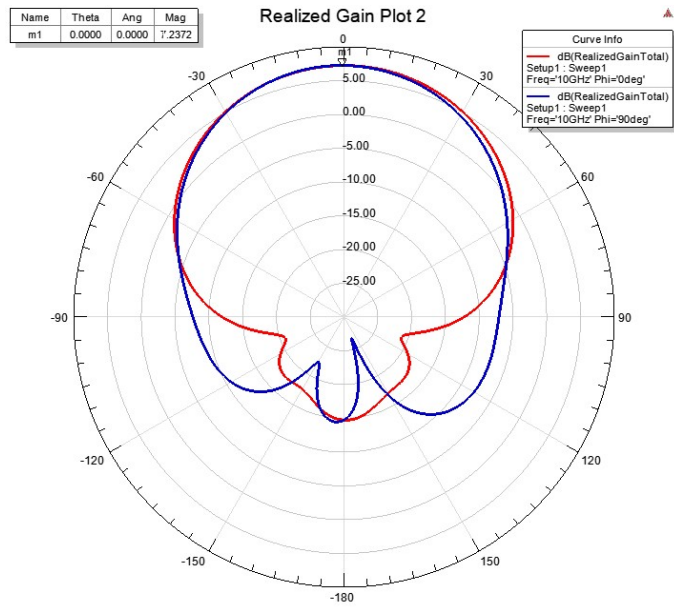Figure 3.4: Average realized gain of the cavity-backed antenna.

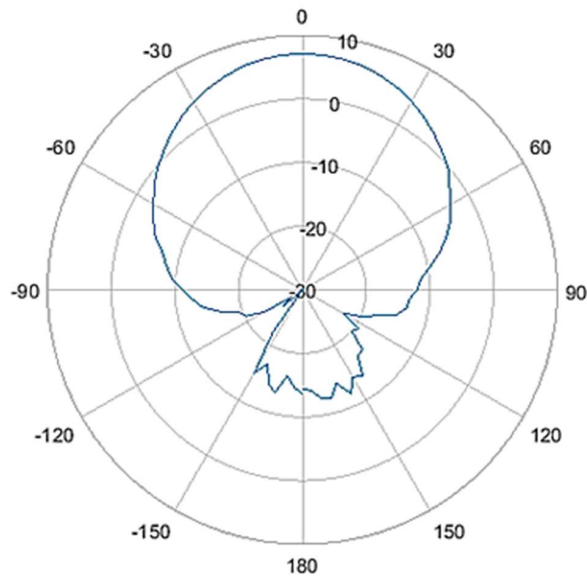Figure 3.5: Simulated E-plane and H-plane radiation pattern of the cavity-backed antenna.

Figure 3.6: Measured H-plane radiation pattern of the cavity-backed antenna.

3.3 Patch Antenna with Embedded Cavity and MMIC Phase Shifter

3.3.1 Substrate Stack-up

Figure 3.7 shows the substrate stack-up of the antenna with embedded phase shifter. Stack-up is similar to the antenna without phase shifter. The 15×10 mm^2 footprint of the cavity enables packaging an MMIC phase shifter within the half-wavelength antenna spacing. TGP2109 8-12 GHz 6-bit digital phase shifter from Qorvo is embedded into the support and cavity substrates by leaving a $4 \times 4 \times 1.64$ mm^3 void through selective FDM of ABS. The phase shifter package is embedded into the support and cavity substrates. Due to the thickness of the phase shifter package, support layer thickness is increased to 0.5 mm. Figure 3.8 shows a snapshot after the phase shifter placement and microdispensing of feed/control lines. The corners of the void are rounded due to the FDM process. This creates difficulty for tightly inserting the MMIC package. To remedy this issue, smaller circular voids at the corners of the main void were created for the MMIC package. This is referred to as ears in Figure 3.8. A tight fit between the MMIC package and void is critical for printing of interconnecting traces to prevent leakage into the substrate and disconnection. The control lines are extended towards the edge of the substrate where through-hole right-angle female sockets are utilized for DC line connections. After the snapshot shown in Figure 3.8, antenna fabrication continues with FDM of 0.25 mm thick ABS layer that forms the microstrip feed line substrate. This substrate layer is slightly retracted around the edges by selective FDM of ABS to fit the sockets in addition to the CPW. This substrate layer also exhibits a 2×2 mm^2 void that corresponds to the middle of the phase shifter. The void facilitates to realize the ground connection of the MMIC package when microdispensing of silver ink is performed over this substrate to form the ground plane. The rest of the fabrication is identical to the antenna without phase shifter. Figure 3.9 shows the photo of the fabricated phased array unit cell with a SMA connector and sockets assembled for measurement.
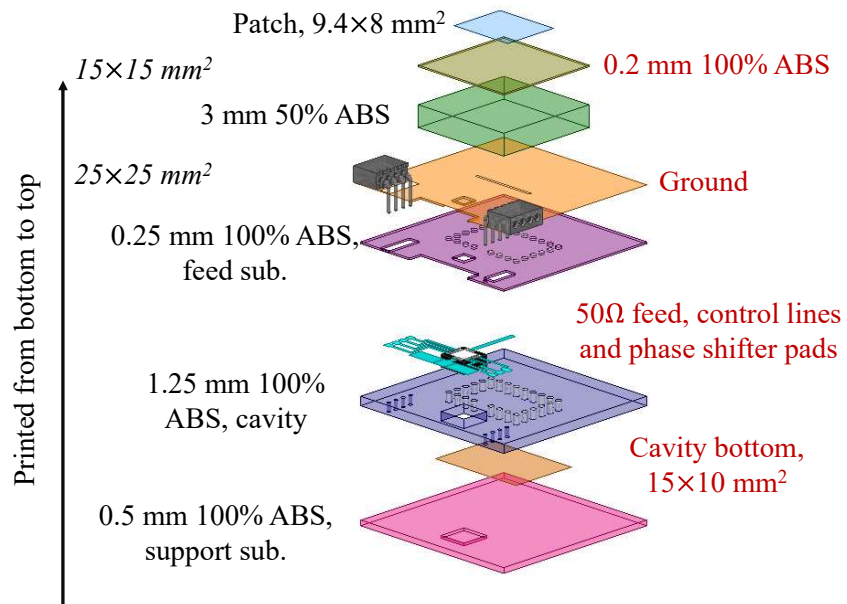
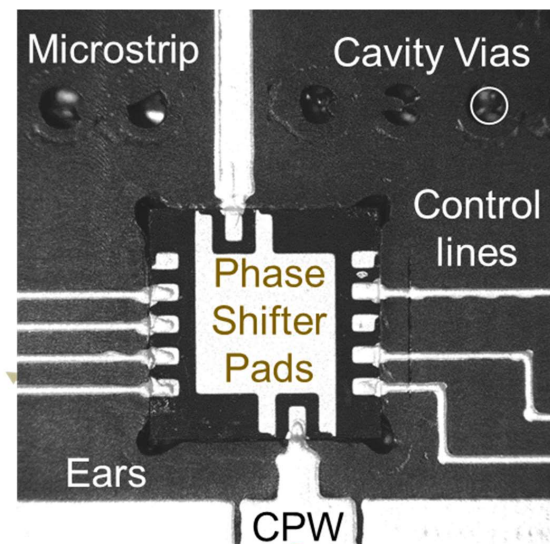Figure 3.7: Substrate stack-up of the antenna with phase shifter.

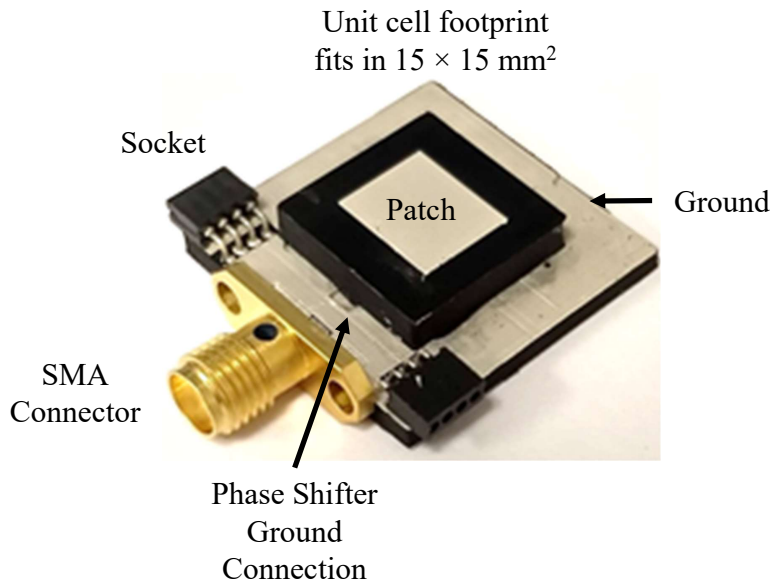Figure 3.8: Snapshot taken after MMIC phase shifter package is placed.

Figure 3.9: Fabricated antenna with embedded cavity and phase shifter.

3.4 Experimental Verification

Antenna with embedded cavity and phase shifter is characterized. Figure 3.10 shows the measured $|S_{11}|$ of the antenna for several phase shifter states. The antenna is well matched and $|S_{11}|$ is less than -10 dB within the operating frequency range. Figure 3.11 demonstrates a realized peak gain for example phase shifter states. The measured realized gain ranges from 0.2 to 2.2 dBi across the 9 – 11 GHz operating band, which is expected due to the 6 dB insertion loss of the phase shifter. Figure 3.12 depicts examples from the phase shift characterization performed through measuring the far-field radiated fields in anechoic chamber. Figure 3.13 shows the measured H-plane radiation patterns at 10 GHz for some phase shifter states. The antenna exhibits more than 20 dB front-to-back ratio, which is similar to the antenna without phase shifter.

3.5 Concluding Remarks

A cavity-backed phased array antenna element with and without embedded MMIC phase shifter is successfully demonstrated using DDM. The antenna without phases shifter operates with 23.8% bandwidth. It has 7.2 dBi realized gain and greater than 80% radiation efficiency including
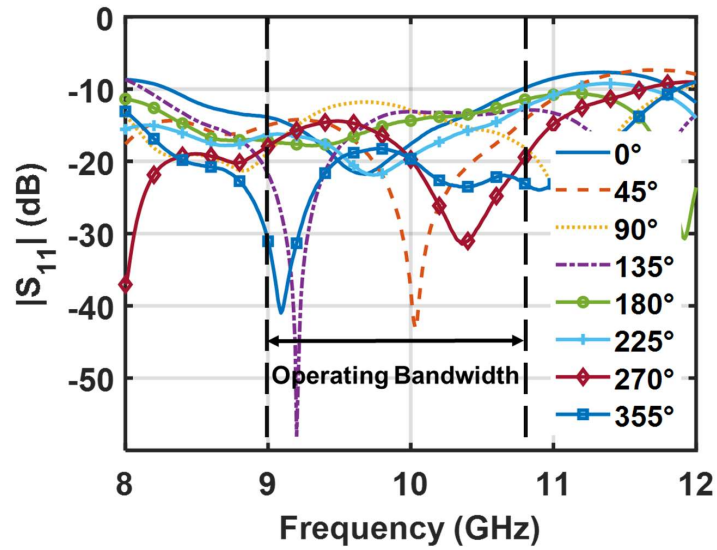
Figure 3.10: Measured $|S_{11}|$ of the antenna with phase shifter.
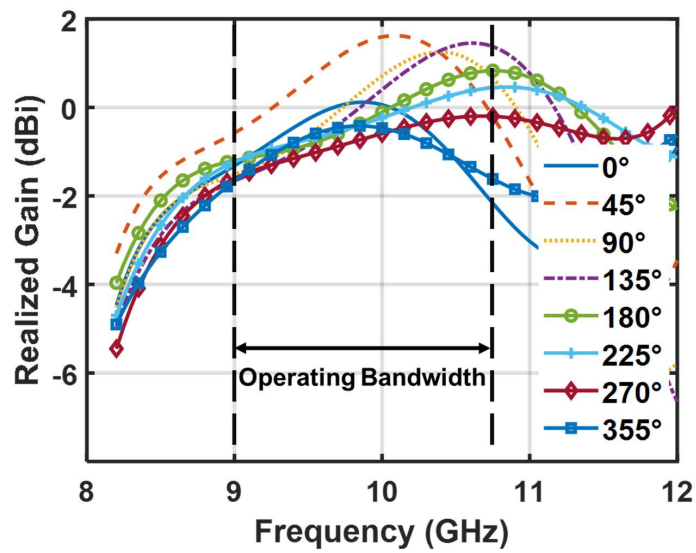
Figure 3.11: Measured average realized gain of the antenna with phase shifter.
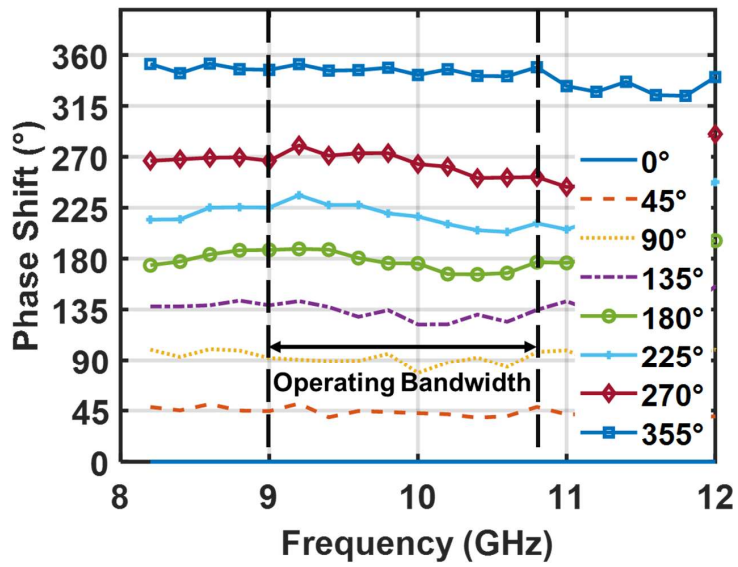
Figure 3.12: Measured phase shift of the antenna with phase shifter.
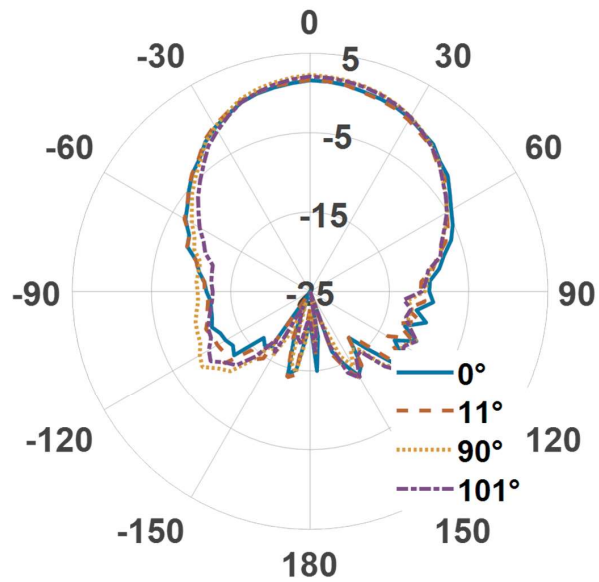
Figure 3.13: Measured 0-2 dBi average gain across bandwidth.

microstrip-to-CPW loss. The phased array unit cell exhibits more than 10 dB return loss within the operating bandwidth and has 0.2-2.2 dBi realized gain due to the loss of the phase shifter. The antenna with embedded MMIC phase shifter is suitable for half-wavelength spacing. In the following chapter, the unit cell design is implemented in a 2×2 sub-array with additional layers to perform the signal, control, and bias line routings. Chapter 4 also provides a literature review on the additively manufactured antennas, antenna arrays and packaging techniques.

Chapter 4: 3D Printed Electronically Scanned Antenna Arrays with Structural Electronics

4.1   Introduction

Phased arrays, also known as electronically scanned arrays (ESA) have many advantages such as fast wide angle coverage without mechanical steering, adaptive beamforming and multiple beams [40]. However, phased arrays are expensive due to costly transmit/receive (T/R) modules, and hard to build at higher frequencies due to half-wavelength spacing (smaller than 18.75 mm $\times$ 18. 75 mm at and above X-band). A major challenge is the need to incorporate many MMICs and ICs within a small unit cell size [40]. Commonly used slat or tile array architectures [41] have high depth, therefore they are not suitable for small platforms such as aircraft and satcom. Planar phased array architectures are more suitable for small platforms due to their low profile, lightweight and low cost [42]. Traditional fabrication techniques such as photolithography require many fabrication steps and platforms. Therefore, they are not cost-effective. Additive manufacturing (AM) can be used to realize monolithic array structure with embedded electronics on a single platform in a one-pass process, potential for low cost fabrication. AM removed the boundaries of traditional fabrication techniques by introducing design flexibilities that can be employed for realizing phased arrays. Antennas with complex geometries or conformal antenna arrays can be monolithically fabricated without special tooling and assembly. AM can be used to build compact and lightweight antennas to satisfy size, weight and power (SWaP) requirements by using low-infill plastic substrates. Dielectric properties and thicknesses of the substrates can be customized by adjusting infill ratio. By using selective printing approach, electronics can be embedded within the package. In addition, metallization can be realized on conformal or inclined surfaces.

Table 4.1 shows the additive manufacturing techniques used for RF devices. The ideal AM technique for an antenna can be determined by material, the complexity of the geometry, and

precision. Antennas with complex geometries are fabricated using stereolithography (SLA), binder jetting, selective laser sintering (SLS), and selective laser melting (SLM). For multilayer antennas with packaged electronics, inkjet/aerosol jet printing or combination of fused deposition modeling (FDM) and microdispensing are suitable.

Table 4.1: Comparison of additive manufacturing techniques.

AM Technique	Materials	Advantages	Disadvantages
Binder jetting	Metal, ceramic or polymer powder and binding agent	High precision, complex shapes	Rough surface, not suitable for multilayer
Selective Laser Sintering	Polymer powder	High precision, suitable for complex shapes	Rough surface, requires post-processing for metallization, not suitable for multilayer
Selective Laser Melting	Metal powder	High precision, suitable for complex shapes	Rough surface, not suitable for multilayer devices
Stereolithography	Photopolymer resin	High precision, smooth surface, suitable for complex shapes	Requires post-processing for metallization, not suitable for multilayer
Inkjet Printing	Dielectric ink, silver nanoparticle ink	High precision, smooth surface, suitable for multilayer	Difficult to realize thick layers, limited material selection, lossy dielectric inks
Aerosol Jet Printing	Silver nanoparticle ink, photopolymers, solvent based polymers	High precision, smooth surface, suitable for multilayer	Difficult to realize thick layers, limited material selection, high dielectric losses
Fused Deposition Modeling	Thermoplastic polymers and ceramic/plastic composites	Custom layer thickness/dielectric properties, moderate dielectric losses, easy to integrate with other AM techniques	Rough surface, low resolution
Microdispensing	Conductive and dielectric inks, pastes	Wide material variety, easy to integrate with other AM techniques	Lower conductivity and resolution

Binder jetting builds the structure by depositing binding agent into the powder. SLS uses laser to sinter polymer power to form the object. SLM, also known as direct metal laser sintering

(DMLS), uses laser to melt metal powder together. SLA forms polymer from photopolymer resin using UV laser. Post-processing might be required for metallization or improving the surface roughness and mechanical strength. Binder jetting, SLS, SLM and SLA can be used to realize high precision monolithic antennas with complex geometries. These geometries are not practical to realize with conventional fabrication techniques. In [3, 4, 43, 44], 3-D fractal antennas and free form antenna with overhanging features and internal gaps using AM are demonstrated. AM enables the experimental verification of these antennas. Similarly, [45] shows a 35 GHz meshed reflector antenna with the illuminating horn, waveguide feed and filter are fabricated monolithically eliminating the need for joints. Design flexibilities of AM can also be harnessed to improve antenna performance. In [3], a 3D Sierpinski fractal monopole antenna using binder jetting and electroplating has wider bandwidth and significantly lower weight compared to the non-fractal version. However, these AM methods are not suitable to integrate with other AM techniques in a single platform. Therefore, they are not suitable for multilayer device fabrication.

For multilayer antennas, inkjet printing (IJP) and aerosol jet printing (AJP) can be used. These techniques use nanoparticle inks, and material selection is limited to low viscosity small particle inks. They provide high precision and smooth surface, which is required for high frequency antennas [7]. However, losses of the photosensitive polymers are significant [46]. Layer thicknesses are also smaller than 10 μm. Multiple passes and dry or cure cycles are required to build thick substrates. Therefore, a LCP laminate can be used as a host substrate as in [7, 47]. Another approach is to use other AM techniques such as FDM for substrates [48]. FDM builds the structure by extrusion of a melted thermoplastic filament, suitable for both thin and thick layers. Although it is not a very high precision method, dielectric losses of the thermoplastic filaments are moderate compared to the dielectric inks used in IJP and AJP. The dielectric losses can be further minimized by decreasing the infill ratio, as shown in [10, 14, 19]. [10] demonstrates a patch antenna with 15% higher radiation efficiency by using a low infill antenna substrate. FDM is easy to integrate with other AM techniques. Microdispensing is used for metallization patterns on planar/conformal surfaces. Wide material selection includes silver nanoparticle inks to conductive pastes with large

particle sizes and high viscosity materials. However, microdispensing is not as high precision as IJP or AJP, and conductivity is lower compared to these techniques.

DDM combines FDM and microdispensing to build multilayer antenna on a single platform. It also incorporates micromachining techniques such as micromilling for surface roughness reduction and laser micromachining for conductivity enhancement [2, 49]. This approach does not require post-processing; therefore, decreases fabrication complexity and potentially decreases fabrication time and cost. In [8], half-wave dipole antenna is embedded into the dielectric structure using DDM, and the balun feed of the antenna is microdispensed on an inclined surface to reduce surface wave losses and size. [9] demonstrates a 2.6 GHz half-wavelength dipole antenna on artificial magnetic conducting (AMC) and low infill substrate using DDM. [14] demonstrates a Ku-band aperture coupled patch antenna with 50% infill antenna substrate, and exhibits 90% radiation efficiency.

Compared to single antennas using AM, there are few 3D printed antenna arrays in the literature. In [11], an 8×8 Ku-band corporate-fed waveguide antenna array is fabricated as a single block using SLM, matching the performance of CNC milling. [12] demonstrates meshed X-band horn antenna and patch antenna arrays using SLM for lightweight applications without significant performance change. In [50], a 2×2 horn antenna array with complex waveguide feed network using SLA and copper plating is demonstrated.

Only two phased arrays using AM are available in the literature. In [13], Ku-band 4-element waveguide phased array using polyjet printing, FDM and copper plating is demonstrated. However, this array is not suitable for installations on small platforms. [13] presents the unit-cell of the first multilayer 2.45 GHz phased array antenna using DDM, which has seven metal layers and seven substrate layers. While the phased array antenna demonstrates the capabilities of AM, it operates at lower microwave frequencies. Higher frequency phased arrays have different challenges such as fitting the components within the small unit cell size and higher precision requirements.

Traditional bulky packaging techniques are replaced by new packaging concepts such as system-on-chip (SoC), system-in-package (SIP), and system on-package (SoP) due to their compact

size, low cost and higher performance [51]. AM offers design flexibilities to achieve smaller packaging and low loss interconnects [52]. Table 4.2 shows novel packaging techniques using AM. In [53], IC die package on a glass slide is integrated with a bow-tie slot antenna using inkjet printed CPW interconnects. Due to the high losses of SU-8, the interconnects have high insertion loss. In [54], a varactor diode integrated with several RF components such as T-line resonator and patch antenna using SLA and damascene process. However, this hybrid approach requires significant post-processing steps (sputtering titanium and copper and etching) for metallization. [55] also follows a hybrid fabrication approach for chip-to-board interconnects. After 0-dB attenuator and MMIC amplifier are inserted into an etched cavity, interconnects are printed using AJP. [56] demonstrates additively manufactured multichip module. Encapsulation with FSS is also printed on chips using SLA and IJP. Inkjet printed interconnects exhibit 3.3 dB higher gain for low noise amplifier over traditional ribbon bonding. In [57], power amplifier in bare die package is attached to molybdenum copper alloy carrier. Substrate and metallization are built up around the package using AJP. [39] presents packaging of MMIC low noise amplifier using DDM. Microdispensed interconnects are laser micromachined for high precision. A hollow package is printed on the IC for protection.

Table 4.2: Comparison of advanced packaging techniques using additive manufacturing.

Reference	Fabrication Technique	Materials	Performance
[53]	IJP	SNP ink, SU-8	~2 dB IL and ~10 dB RL at 30 GHz
[54]	SLA, damascene	Acrylic photopolymer, copper	0.78 dB IL at 7 GHz
[55]	Photolithography, AJP	LCP laminate, UV curable epoxy, SNP ink	0.15 dB at 40 GHz
[56]	IJP, SLA	SNP ink, SU-8, resin	~3 dB IL and ~10 dB RL at 40 GHz
[57]	AJP	Polyimide, barium titanate, silver ink	~1 dB IL at 15 GHz
[39]	DDM, laser micromachining	ABS, silver paste	~2.4 dB IL at 20 GHz
Work in Chapter 2	DDM	ABS, silver paste	0.12 dB IL and 33 dB RL at 20 GHz
[37]	DDM	ABS, silver paste	–

In Chapter 2, an MMIC phase shifter is placed on a ground plane of a dual-polarized antenna using DDM. By optimizing the ramped transitions, the interconnects exhibit 0.12 dB simulated insertion loss and more than 33 dB simulated return loss up to 20 GHz. In Chapter 3, we successfully demonstrated the X-band aperture-coupled patch antenna with embedded cavity and MMIC phase shifter. Embedding of MMIC phase shifter allows smaller packaging required for planar phased array architecture. In this chapter, we demonstrate a 2×2 sub-array for phased array realizations, which is an extension to the phased array unit cell.

4.2 2×2 Sub-array Design

Figure 4.1 shows substrate stack-up of the 2×2 sub-array. A major challenge of the sub-array design is a large number of control and bias lines that need to enter each unit cell which is 28 in total. To reduce this, a shift register is utilized in each unit cell along with the phase shifter. This approach reduces the control bias lines to 8. Due to unit cell size, it is not possible to keep phase shifter and shift register in the same layer. Hence, the phase shifter is taken below the cavity with vertical feed transition across the cavity edge as it can be seen in Figure 4.2. Figure 4.3 shows the unit cell of the sub-array. The design is 37 x 36 mm^2. Overall thickness is 6.9 mm. The sub-array exhibits seven metal layers and eight dielectric layers.

The sub-array is simulated without the phase shifters but with entire feed network and control lines. Figure 4.3 shows the 3D broadside radiation pattern of the sub-array. It exhibits 7.8 dBi realized broadside gain, while 2 dB loss comes from the feed network. The feed network loss of the sub-array in a larger array is lower since the signal will be brought from its center. Currently, RF signal enters from the side to utilize an edge connector, which causes extra transmission line length. The sub-array has $|S_{11}|$<-10 dB within 9-11 GHz bandwidth.

4.3   Concluding Remarks

A detailed literature review on antennas, phased arrays using additive manufacturing in the recent literature is presented in this chapter. Novel IC packaging techniques using AM are also
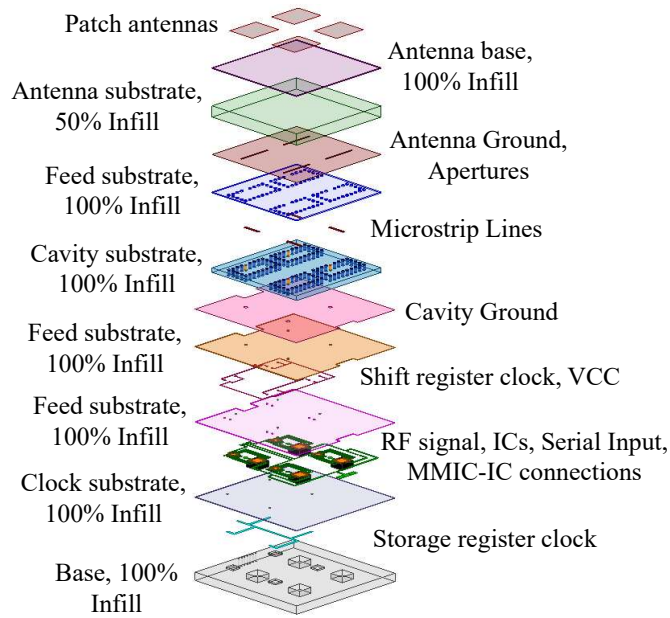
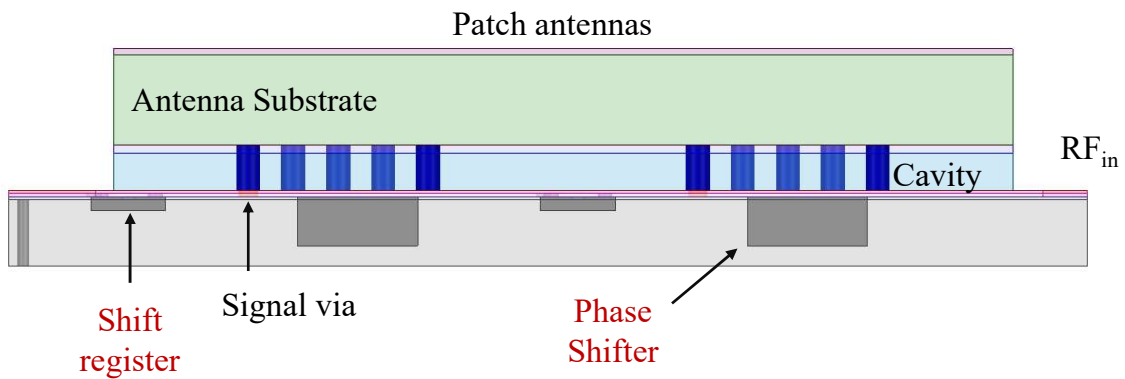Figure 4.1: Substrate stack-up of the 2×2 sub-array.
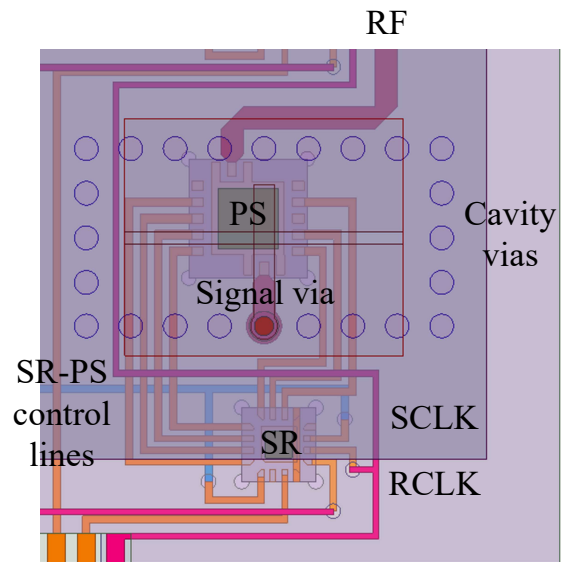

Figure 4.2: Side view of the sub-array.

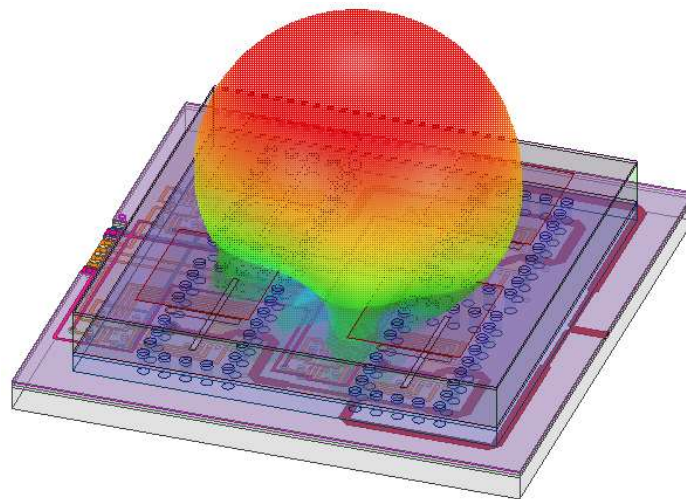Figure 4.3: Top view of the sub-array unit cell.

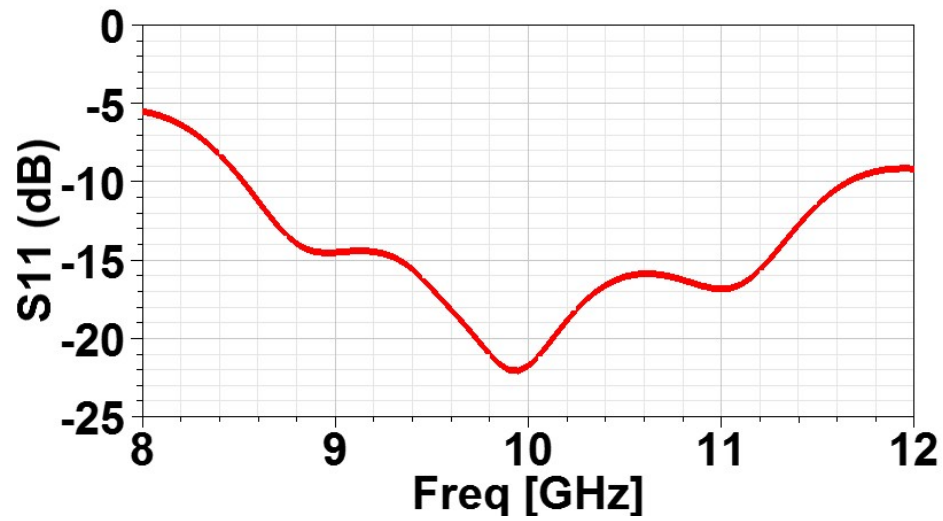Figure 4.4: 3D radiation pattern of the sub-array.

Figure 4.5: Reflection coefficient of the sub-array.

discussed for planar and conformal phased array architectures. The 2×2 sub-array design based on the phased array unit cell and its simulated performance is also demonstrated. The fabrication and experimental verification of sub-array implementation are carried out. However, the results of these studies are not available to the public yet.

Chapter 5: Conductivity Improvement of Microdispensed Microstrip Lines and Grounded Coplanar Waveguides Using Laser Micromachining

5.1 Introduction

Metal deposition is one area where AM techniques can provide advantages over conventional fabrication methods[3]. For example, AM can reduce the number of fabrication steps and does not require special tooling such as masks needed in photolithography. AM also allows realizing electronics on conformal surfaces. However, the efficiency of high frequency microwave devices continues to be a concern due to the high losses of dielectric and conductive materials used in AM techniques. Chapter 2 demonstrated low-loss transmission line design by harnessing design flexibilities of DDM. However, conductor losses are still significant due to low conductivity of silver inks/pastes. Silver nanoparticle (SNP) and flake based inks and pastes provide less than 10% of the conductivity of copper [13, 30].This chapter presents techniques to minimize conductor losses for different type of transmission lines. AM techniques such as selective laser melting (SLM) or direct metal laser sintering (DMLS) provide higher conductivity by melting and fusing or sintering the metallic powders. However, SLM and DMLS techniques are not suitable for multilayer devices. Inkjet printing (IJP), aerosol jet printing (AJP) and microdispensing are the AM techniques suitable for realizing metallizations in multilayer device structures. IJP and AJP provide smaller feature sizes and thin layer thicknesses as compared to microdispensing. On the other hand, microdispensing can be used as a thick film process and it is easy to integrate with fused deposition modeling (FDM)

---

to develop a stand-alone AM platform for multilayer device realizations [58]. However, due to the low glass transition temperature of thermoplastic polymers often used in FDM process (and also in IJP and AJP processes), the SNP inks and pastes are typically cured or dried below the optimum temperatures. This exacerbates the conductor loss issue even further, as optimally cured SNP inks/pastes already exhibit <10% of copper conductivity. Photonic curing, laser and thermal sintering are techniques that are being investigated to improve the conductivity [27, 59–63] of SNP inks/pastes by transforming the physical structure from particles/flakes into a solid. Alternatively, the work in [2] proposes to improve conductivity of microdispensed transmission lines (TLs) using laser micromachining. The concept was investigated for coplanar waveguide (CPW). It was observed that laser micromachining not only improves the minimum achievable feature size of the CPW slots, but also enhances the conductivity by solidifying the silver particles within the paste at the edges of the slots. However, the study in [2] was limited to CPW lines and the selected CPW line geometry was tightly coupled to the ground plane, thus suffering from extremely high losses. It is well-known that conductor loss depends on the TL type and geometry. It is therefore important to investigate the use of laser micromachining for other type of microdispensed TLs and discover the limits of the achievable improvements in conductivity. Consequently, this letter aims to investigate the laser micromachining for the first time for microstrip and grounded CPW (GCPW). Laser micromachining is found to improve the conductivity of the lines within the 1 GHz – 30 GHz frequency band. Scanning electron microscope (SEM) images and optical profilometer data is utilized to explain the physical reasoning behind the conductivity improvement of the microdispensed TLs. Conductivity improvement for microstrip lines exhibiting different substrate thicknesses and varying GCPW width/slot ratios are reported.

5.2 Fabrication

Microwave characterizations are performed by utilizing test fixtures prepared on a planar substrate (254 μm, RO3035, $\varepsilon_r = 3.6$, tanδ=0.0018). Standard printed circuit board (PCB) manufacturing is utilized for the generation of probe pads, through-reflect-line (TRL) calibration standards,

and ground planes from 35 μm thick copper with electroless nickel immersion gold (ENIG) plating. The test fixtures allow to isolate and investigate the conductor loss of signal traces in microdispensed microstrip line and GCPW. Signal traces are microdispensed between the probe pads using CB028, which is a flake-based silver paste from Dupont. The nScrypt SmartPump along with a 3Dn-Tabletop printer is the tool utilized in microdispensing process. Refrigerated paste is spun at 2000 rpm for 5 min to obtain a homogeneous mixture and left at room temperature for an hour for viscosity stabilization. Ceramic dispensing tip with 75 μm inner and 125 μm outer diameters is selected since it is found to provide a consistent single pass trace width of 125 μm, which is satisfactory to generate the signal trace widths investigated in the presented work.

A main challenge in high frequency microwave device fabrication is the requirement for precise control over the dimensions of the signal traces. Hence the microdispensing speed and pressure values were iteratively investigated to achieve the 125 μm single pass trace width. 2 psi pressure with 2 mm/sec printing speed is determined to be proper for providing adequate CB028 flow from the microdispensing tip nozzle. In addition, the gap between the microdispensing tip and substrate surface is kept between 30 μm and 40 μm to achieve the signal trace width. Following the completion of microdispensing, CB028 on the test fixture is dried at room temperature for 20 min to evaporate some of its solvent. Afterwards, the test fixture is placed in a hot air oven for drying with manufacturer recommended drying conditions at 160°C for an hour to achieve the highest possible conductivity.

Figure 5.1 shows the 50 Ω microstrip line and GCPW with microdispensed signal traces. Line width, thickness and roughness profile were measured with a Wyko NT9100 non-contact nanometer scale optical profilometer. The thickness at the center of the signal trace is 17 μm. Cross sections of microdispensed lines are trapezoidal due to the spreading of CB028 on the substrate. Figure 5.2 shows the trapezoidal shape of the microstrip line measured with profilometer. All dimensions are in μm. The base of the trapezoid is 250 μm wider than its top edge. The edge angle is 7.8°. GCPW exhibits the same edge angle. Line widths are indicated with respect to the trapezoidal base width. Line width for the microstrip line and GCPW are 546 μm and 432 μm,
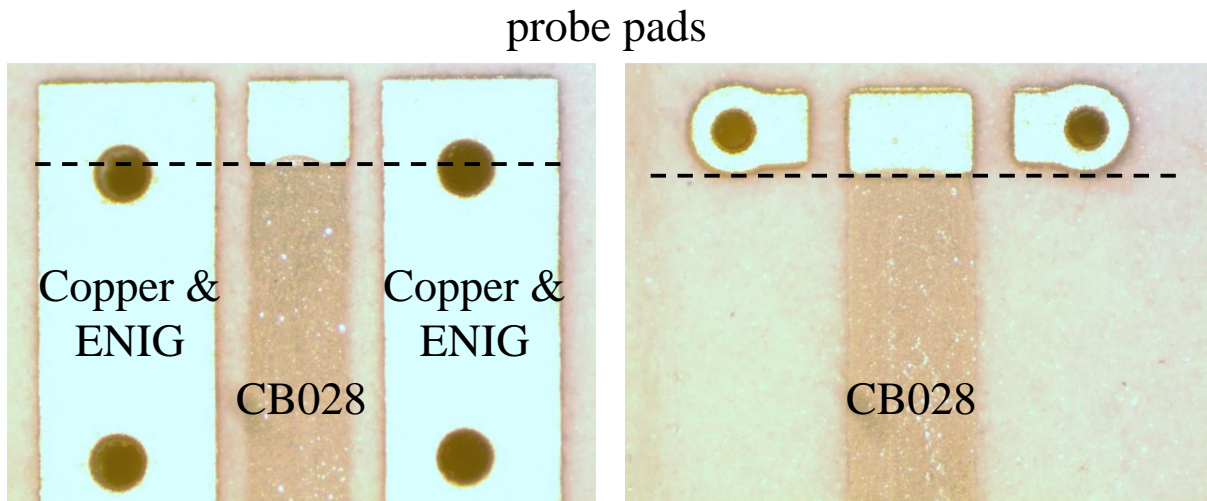
probe pads

Figure 5.1: Microdispensed GCPW and microstrip line.
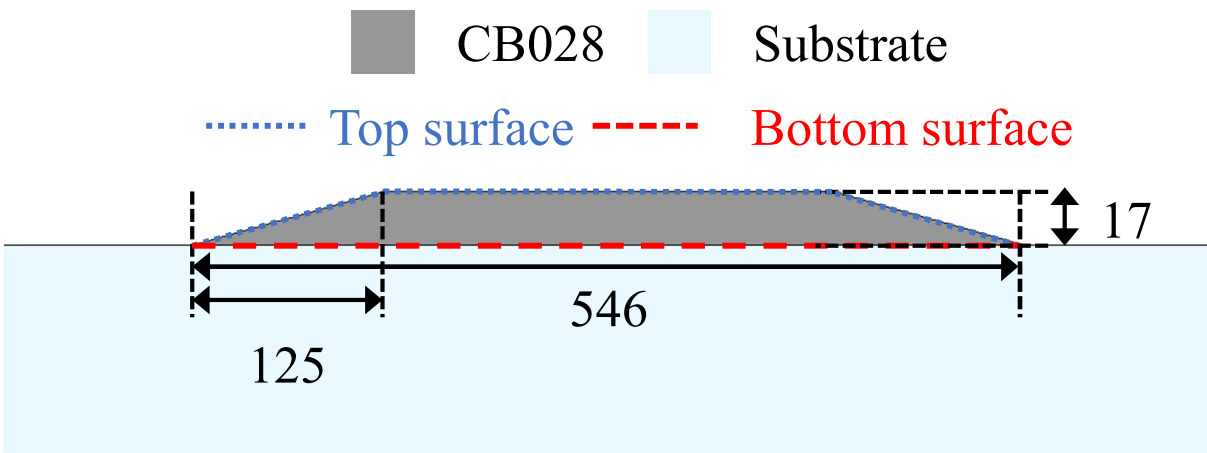

Figure 5.2: Cross-section of microdispensed microstrip line.
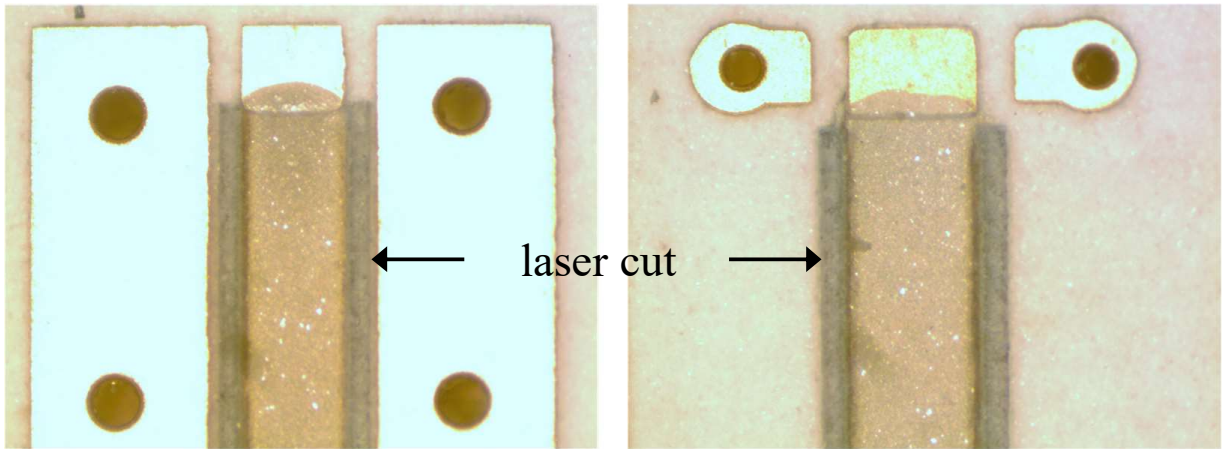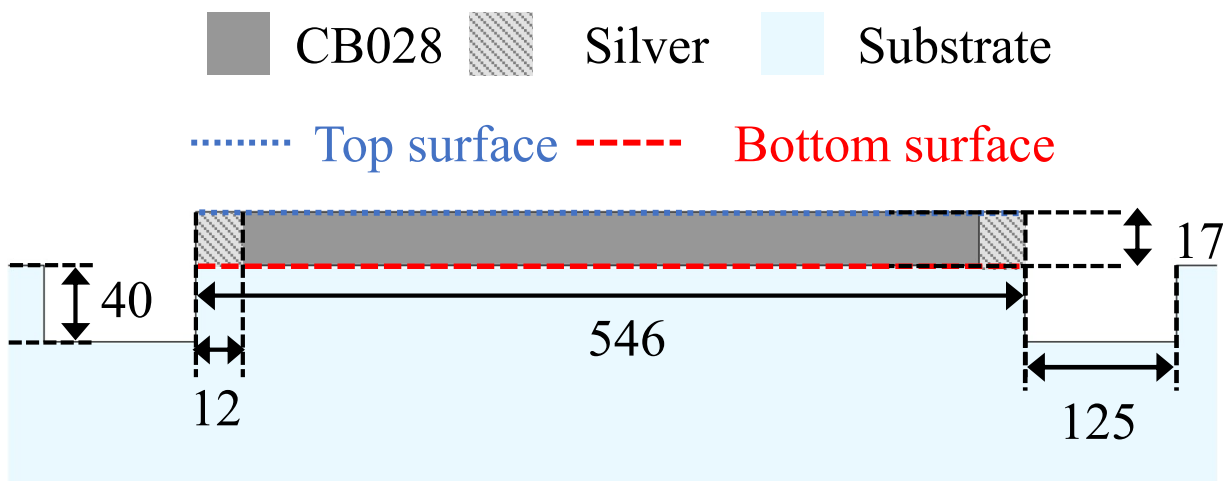
Figure 5.3: Laser micromachined GCPW and microstrip line.

Figure 5.4: Cross-section of laser micromachined microstrip line.

respectively. GCPW slots are 152 μm wide. Arithmetic average roughness (Ra) and root mean squared roughness (Rq) along the center of the line are 0.7 μm and 0.84 μm, respectively. Ra and Rq along the tapered edge are 0.92 μm and 1.15 μm, respectively. Rq of the bottom surface of the signal trace is equal to 2.1 μm.

Figure 5.3 shows the laser micromachined microstrip line and GCPW. Signal lines are microdispensed 250 μm wider than 50 Ω line widths given above. A 1064 nm Nd: YAG pulsed picosecond laser is used to cut/remove 125 μm wide CB028 from each edge of the lines. Figure 5.4 shows the rectangular cross-section of the microstrip line and substrate removal after laser
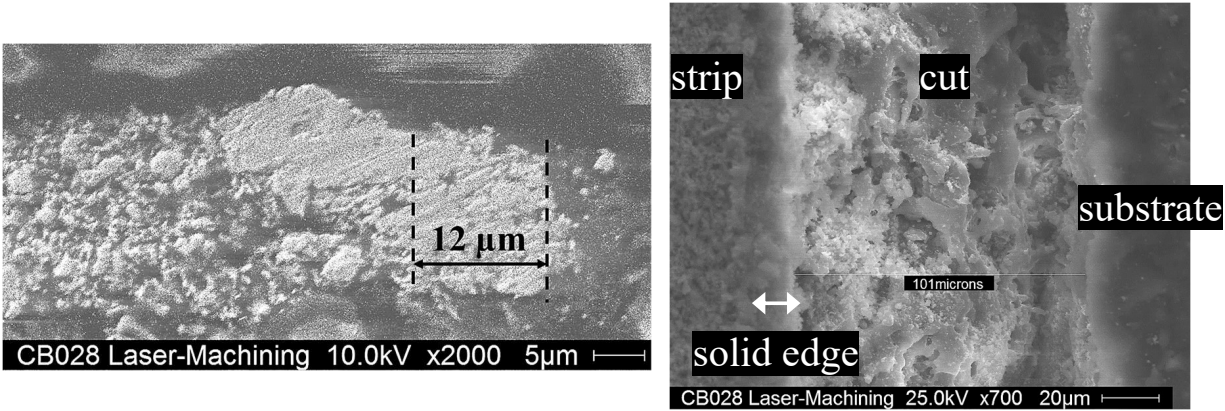
Figure 5.5: SEM images of cross-section (left) and top view (right) of laser micromachined microstrip line.

micromachining. All dimensions are in μm.The cross-section before laser micromachining is the same shape as Figure 5.2, while the line width is 250 μm wider. The measured widths for the micromachined lines are 533 μm and 406 μm for the microstrip line and GCPW, respectively. GCPW slots are 165 μm wide. Laser micromachining is performed with a 10 μm single pass width by setting scanning speed to 25 mm/s, energy to 2 MW and repetition rate to 100 kHz. Although laser parameters are optimized for the substrate, the laser still cuts 40 μm into the substrate due to the substrate's absorption at 1064 nm. The thickness roughness profile is identical to that of the microdispensed line at the center. Despite small dimensional variations in line widths due to different printing process (i.e. with or without laser micromachining), all lines exhibit near 50 Ω impedance and very well matched in measurements, as shown in Section III. Hitachi S-800 Scanning Electron Microscope (SEM) images obtained from a laser micromachined microstrip line are shown in Figure 5.5. The line edges are perpendicular to the substrate surface. Similar to what has been observed in CPW [2], CB028 is formed into solid silver at the line edges due to the residual heat as laser micromachining is removing the adjacent material. The solidified edge width is 12 μm. The conductivity of this region can be assumed to be identical to solid silver at 61 MS/m.

5.3 Characterization

The S-parameters of the TLs were characterized using a Keysight N5227A PNA Microwave Network Analyzer, 650 μm pitch ground-signal-ground probes from GGB, and a portable probe station from Cascade Microtech. The effect of probe pads on the measurement data was removed by shifting the reference plane using TRL standards. Delay lines are 1.02 mm, 3.1 mm, and 7.82 mm longer than thru standard. WinCalXE software was used for the TRL calibration.

Figure 5.6 shows S-parameters of the measured and simulated microstrip lines and GCPWs before and after laser micromachining. Multiple TLs were measured, and similar results were achieved. Return loss of all measured lines is higher than 20 dB, implying mismatch losses are less than 0.04 dB. Laser micromachining significantly reduces the insertion loss (IL) of both TLs. IL improvement starts at low frequencies since the solidified edge width is larger than the skin depth at 1 GHz (7.4 μm for CB028). At 30 GHz, IL decreases by 0.18 dB/cm for microstrip and 0.29 dB/cm for GCPW. Laser micromachined microstrip gives the lowest IL, while GCPW without laser micromachining has the highest IL.

Table 5.1 compares the attenuation of planar TLs and conductivities reported in the literature. In [64], IJP 0.9 μm thick ML on 75 μm Kapton tape is sintered at 200°C inside the oven. In [27], 16 μm thick CPW on 50 μm LCP is sintered at 140°C on a hot plate for several hours. However, thermal sintering methods require long post-processing times and puts thermal load on the substrates [60] and embedded electronics. In [61], conductivity after selectively laser sintering the SNP ink is characterized using ring resonators. In [62], conductivity of AJP 2 μm thick ML on 30 μm SU-8 is improved using IR laser sintering. [2] demonstrates significant conductivity improvement on tightly-coupled 25 μm thick CPW on 0.38 mm Rogers RT5870 by melting the edges. [65] applies the same technique to 25 μm thick CPW on 0.5 mm ABS with 20 μm slots between the conductors. The laser micromachined lines investigated in this dissertation show the best IL performance. This is partially due to the TL type and partially due to enhanced conductivity achieved with the laser micromachining.
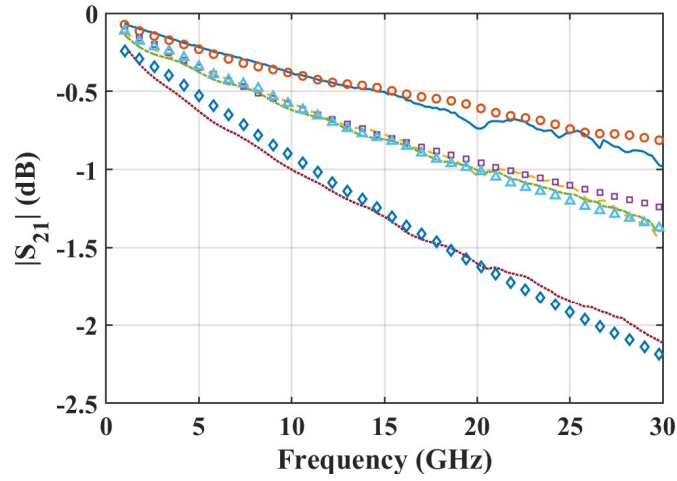
Figure 5.6: $|S_{21}|$ (dB) of 25.4 mm long microdispensed and laser micromachined microstrip lines and GCPWs.
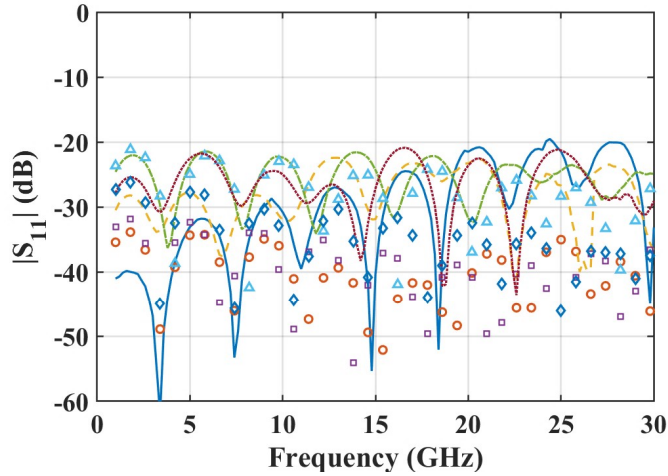
Figure 5.7: $|S_{11}|$ (dB) of 25.4 mm long microdispensed and laser micromachined microstrip lines and GCPWs.

Table 5.1: Comparison of different conductivity improvement techniques.

Ref.	Fabrication Technique	Insertion Loss (dB/cm)	Conductivity (MS/m)
[64]	IJP, thermal sintering	Microstrip line (ML) 4.5 at 5 GHz	10.6 at DC
[27]	AJP, hot plate sintering	CPW 0.9 at 30 GHz	37.8 at DC
[61]	IJP, laser sintering	—	6.48 at 15 GHz
[62]	Microdispensing, laser micromachining	ML 3 at 18 GHz	17 at DC
[2]	Microdispensing, laser micromachining	CPW 0.8 at 20 GHz	10 at 20 GHz
[65]	Microdispensing, laser micromachining	CPW 1.3 at 30 GHz	—
This work	Microdispensing, laser micromachining	ML 0.4 at 30 GHz	ML 5 at 30 GHz
This work	Microdispensing, laser micromachining	GCPW 0.55 at 30 GHz	GCPW 12.5 at 30 GHz

5.4 Modeling

Full-wave electromagnetic simulations with Ansys HFSS v19.2 are utilized to extract the effective conductivities of the TLs, understand the factors that contribute to performance enhancement, and predict the potentially achievable performance when different line widths are needed. HFSS models are based on the line geometry and material composition observed with profilometer and SEM image measurements reported in Section 5.2. Modeling the top and bottom surface roughness of the signal trace is critical for accurate modeling. CB028 conductivity is taken as its DC conductivity obtained when drying at 160°C as 4.63 MS/m [13]. For solidified CB028 regions, conductivity of silver is used which is 61 MS/m. Figure 5.6 shows the full-wave simulated vs. measured transmission coefficient of 25.4 mm long lines. Excellent agreement is obtained between the simulations and measurements – verifying the accuracy of the simulation model. Following this agreement, TL models with perfect rectangular cross-sections and uniform conductivities are utilized to extract effective conductivity values for the laser micromachined lines. For perfectly shaped TL models, top surface roughness is not included; therefore, IL associated with top surface roughness of microdispensed lines contributes to a lower effective conductivity. On the other hand,

bottom surface roughness is kept for the model since this is determined by the substrate material. At 30 GHz, effective conductivities of microdispensed microstrip line and GCPW are 1 MS/m and 0.9 MS/m, respectively. Effective conductivities of laser micromachined microstrip line and GCPW are 5 MS/m and 12.5 MS/m, respectively.

HFSS models with full details of material and line cross-section non-uniformities are then utilized to identify the factors that contribute to the IL reduction. The loss factors are compared for microdispensed and laser micromachined TLs.

1) Dielectric loss: For the microstrip line, the 40 μm-deep cuts made in the substrate during the laser micromachining are not critical since dielectric loss decreases only by 0.01 dB/cm at 30 GHz due to the substrate removal with laser micromachining.

2) Surface roughness loss: IL associated with surface roughness decreases by 0.07 dB/cm at 30 GHz for the microstrip line. This is due to the smaller surface area of the laser micromachined line and change in current distribution due to removal of tapered edges. For the GCPW, IL associated with surface roughness decreases by 0.1 dB/cm with laser micromachining.

3) Conductor loss: For the microstrip line, the remaining 0.1 dB/cm IL improvement at 30 GHz is associated with conductivity enhancement. Switching from a trapezoidal to a rectangular cross-section improves IL by 0.02 dB/cm. Inclusion of higher conductivity regions provides an additional 0.08 dB/cm IL improvement. For GCPW, conductor loss decreases by 0.22 dB/cm (0.02 dB/cm from cross-section, 0.2 dB/cm from conductivity). Since GCPW current is more concentrated at line edges, it benefits more from laser micromachining compared to microstrip line.

Figure 5.8 shows the IL improvements that can be achieved with laser micromachining for varying line widths. Numbers in the legend denote signal line widths. TL impedance is kept at 50 Ω. Hence, microstrip lines are over 127 μm and 508 μm thick substrates with 267 μm and 1070 μm line widths, respectively. GCPWs are kept on the original 254 μm thick substrate with 51 μm and 305 μm slot widths corresponding to 295 μm and 533 μm line widths, respectively. At 30 GHz, IL improvement is 0.41 dB/cm for the GCPW and 0.39 dB/cm for the microstrip line exhibiting the narrowest line width. It is observed that narrower lines benefit more from the laser
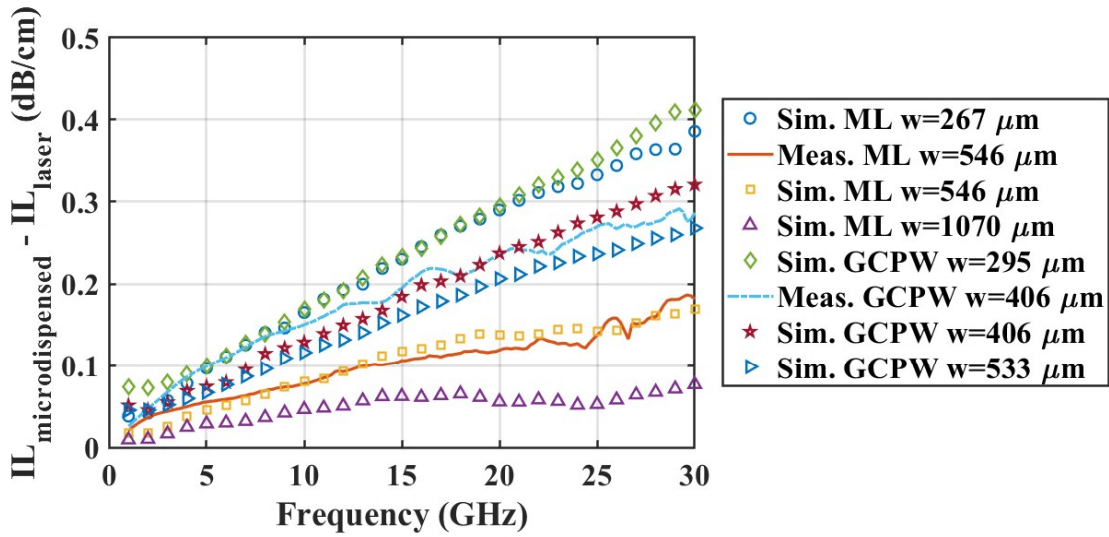
Figure 5.8: Insertion loss improvement with laser micromachining.

micromachining. This shows that laser micromachining will be quite important for realizing chip to package interconnects [39] not only from the feature size, but also from IL perspectives.

5.5 Concluding Remarks

The effect of laser micromachining on the IL and effective conductivity of microdispensed microstrip line and GCPW is investigated for the first time. On a 254 μm thick ε_r = 3.6 substrate, 30 GHz IL of laser micromachined 50 Ω microstrip line and GCPW are shown to be 0.18 dB/cm and 0.29 dB/cm lower than their microdispensed counterparts. Effective conductivity of laser micromachined microstrip line at 30 GHz is 5x of its microdispensed counterpart. Laser micromachining is shown to provide 13x improvement for effective conductivity of the GCPW. It is proven that while laser micromachining is most beneficial for improving the effective conductivity of microdispensed GCPWs exhibiting narrower signal traces, microdispensed microstrip lines can also greatly benefit from the employment of laser micromachining process.

Chapter 6: Concluding Remarks

In this dissertation, 3D printed antennas and phased arrays with structural control electronics are demonstrated. The antennas are designed to be utilized in a half-wavelength spacing at X-band and Ku-band. Packaging of control electronics within a small unit cell is achieved by structural embedding. Design flexibilities of DDM such as custom material compositions, shapes, metallization patterns are harnessed to realize high radiation efficiency and wideband antennas with structurally embedded electronics. High performance of the antennas is achieved by utilizing low infill antenna and feed substrates. Transmission line losses are also investigated for minimizing feed network losses of the antenna arrays and thus increase radiation efficiency. Specifically, this dissertation demonstrates

- capabilities of DDM to realize multilayered RF devices with advanced packaging techniques.

- the lowest fully printed transmission line loss reported in the literature. By customizing material properties and substrate thickness, the microstrip feed line exhibits 0.25 dB/cm insertion loss at 18 GHz.

- a wideband Ku-band dual-polarized stacked patch antenna with embedded MMIC switch. The antenna exhibits 6.3 dBi realized gain at 15 GHz, >80% radiation efficiency, and 45% $|S_{11}|$ <-10 dB bandwidth. MMIC switch is embedded within the feed substrate and connected to feed lines through 3D interconnects.

- a novel MMIC switch integration technique with 3D interconnects enabling more than 33 dB return loss and compact packaging for 2D array applications.

- an X-band phased array antenna unit cell with embedded cavity and MMIC phase shifter. The antenna exhibits 23.8% $|S_{11}|$ <-10 dB bandwidth, 7.2 dBi realized gain at 10 GHz, and 80% radiation efficiency without including phase shifter loss.

- a 2×2 sub-array implementation of the unit cell. Each unit cell includes a shift register IC for controlling phase shifter therefore significantly reducing the number of control lines.

- laser micromachined microstrip line and GCPW. Effective RF conductivity improvement with laser micromachining is 5× for microstrip line and 13.9× for GCPW.

Structural integration of MMICs and ICs in QFN packages within a small unit cell is suitable for passive electronically scanned arrays (PESAs). The industry is moving towards active electronically scanned array (AESA) and digital phased array technology [41]. Each unit cell in these arrays includes a transmit/receive (T/R) module. The current approach is to use a slat or tile (also known as plank) array architecture, where the T/R module is connected perpendicular to the antenna [41], resulting in significant depth. The demand for using AESAs in small platforms such as aircraft, satellite communications on-the-move (SOTM), and 5G communications is increasing. Small size, lightweight, high power and low cost (also known as SWaP-C) are the most important design requirements for these applications [42]. Fitting multiple MMICs and ICs (whole T/R module) remains to be challenging [40]. For the planar phased array applications, design flexibilities of additive manufacturing can provide many advantages over the conventional fabrication methods. What follows is the list of future on additively manufactured antennas, phased arrays and RF devices.

6.1 Planar Transmission Lines

Additively manufactured planar transmission lines still have higher losses compared to the transmission lines fabricated with conventional fabrication methods such as photolithography. Conductor losses are the major loss factor. The conductor losses are higher with 3D printed metallization due to the low conductivity of silver inks/pastes. Post-processing techniques such as laser

micromachining, laser sintering, photonic curing and thermal sintering have been used to improve the effective RF conductivity of printed silver inks/pastes. While laser micromachining increases conductivity to conductivity of bulk silver, its effect is local. While the effect of laser sintering, photonic curing and thermal sintering on conductivity is not as significant as laser micromachining, their effect is over all metallization. Therefore, combining these post-processing techniques can further enhance conductivity. The surface roughness of additively manufactured substrates can also increase transmission line losses significantly at higher microwave frequencies. For instance, FDM causes waviness on the surface. Surface micromachining techniques such as micromilling and [37] and thermal and vapor smoothing [66] can reduce surface roughness. Dielectric losses of printed dielectric inks are significantly higher than standard LCP or PTFE laminates. Printed thermoplastic polymers have moderate dielectric losses. Thermoplastic polymers such as polyetheretherketone (PEEK) has lower loss tangent compared to ABS.

6.2 Interconnects

Printed interconnects can provide many advantages over conventional fabrication methods such as the switch transition used in Chapter 2. Improving the robustness and flexibility of the interconnects is crucial against harsh environmental conditions. Printed via performance is important for multilayer device fabrication [67, 68]. Therefore, high-aspect-ratio via performance using additive manufacturing should be investigated to achieve performance similar to PCB fabrication techniques.

6.3 Connectors

Connectors can be fabricated and embedded within the package using additive manufacturing. This method can be used to minimize the reflection at the connector launch. Also, connectors optimized for additively manufactured multilayer RF devices can be fabricated with metal printing techniques such as DMLS or SLM.

6.4 Active Electronically Scanned Arrays

The typical lateral size of the QFN MMIC packages is 4 mm $\times$ 4 mm, while unit cell sizes at and above X-band are less than 18.75 mm $\times$ 18. 75 mm. When the routing of RF and control lines are included, it is not possible to fit the entire T/R module formed of MMICs within the unit cell. Therefore, beamformer ICs, also known as core chips, provide a small size for phased array applications by fitting the entire T/R module into an IC. The ADAR1000 X-/Ku-Band Beamforming Chip from Analog Devices, which has 7 mm $\times$ 7 mm lateral size is an example for the beamforming ICs. Phased array antennas with embedded beamformer IC using additive manufacturing should be investigated. This would be the first active phased array using additive manufacturing in the literature.

6.5 Power Handling

Commonly used thermoplastic polymers used in the FDM processes such as ABS and PLA are easy to print. However, they have low glass transition temperatures. In order to integrate power amplifiers with additively manufactured antennas, higher temperature thermoplastic polymers such as Ultem, PEEK, or polyether ketone ketone (PEKK) can be used for fabrication. Also, using higher conductivity silver inks or pastes decreases conductor losses and improves thermal management. Other additive manufacturing techniques such as DMLS or SLM can also be integrated for heat sink fabrication. The power handling limitations of additively manufactured RF devices should be investigated.

6.6 Conformal Antenna Arrays

Compared to planar antenna arrays, conformal arrays have many advantages, such as maintaining the radiation pattern at high scan angles, and wider scan angles [69]. Additive manufacturing can be used to fabricate antennas directly on the conformal platform, reducing aerodynamic drag. It enables truly conformal array geometry compared to sector arrays.

$\sim 133 \times 128 \text{ mm}^2$
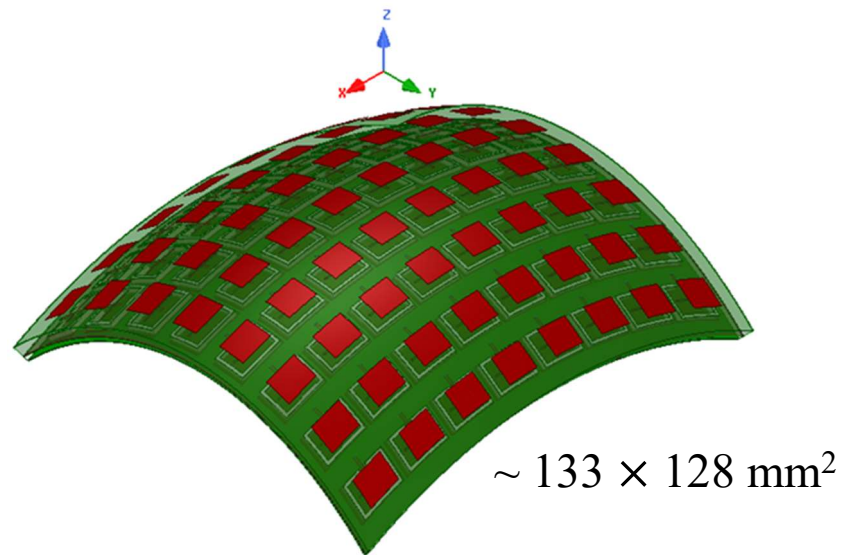
Figure 6.1: Conformal 8x8 antenna array on doubly curved surface.

Figure 6.1 shows the conformal cavity-backed phased array model. The 8x8 array is doubly curved on the surface. Fabrication of this antenna with traditional fabrication techniques is not practical. The antenna is simulated in Ansys HFSS. 50 Ω lumped ports are used to excite the antennas. Figure 6.2 shows the broadside radiation pattern of the antenna. Phases of the antenna elements are corrected to arrive at the reference plane with the same phase. The array exhibits 22 dBi broadside realized gain. The radiation efficiency of the array without including the feed distribution network is 86%. Mutual coupling between the antenna elements is less than -17 dB. The antenna has 20% $|S_{11}|$<-10 dB bandwidth. Traditional 3-axis printers cannot be used for the fabrication of conformal arrays. In addition to 3-axis, two rotary axis motion is required to enable conformal printing.
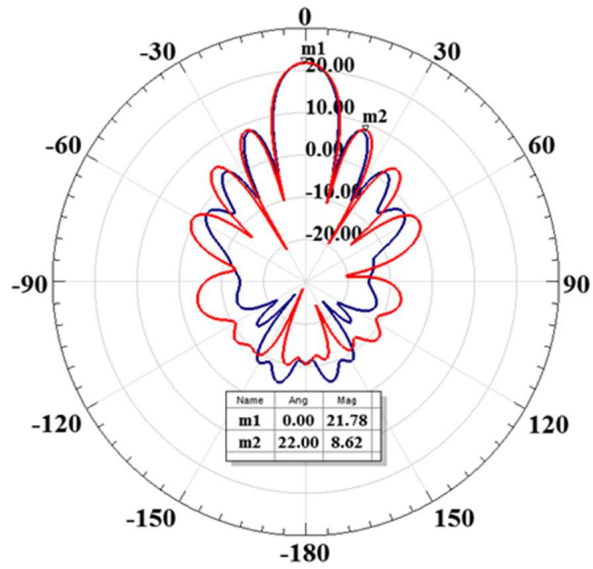
Figure 6.2: Broadside radiation pattern of the conformal array.
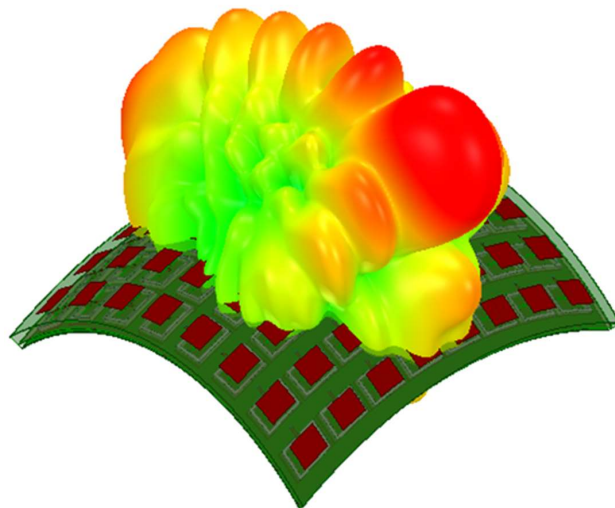
Figure 6.3: 3D radiation pattern of the conformal array at high scan angle.

References

[1] R. Sorrentino and O. A. Peverini, "Additive manufacturing: a key enabling technology for next-generation microwave and millimeter-wave systems [point of view]," *Proceedings of the IEEE*, vol. 104, no. 7, pp. 1362–1366, 2016.

[2] E. A. Rojas-Nastrucci, H. Tsang, P. I. Deffenbaugh, R. A. Ramirez, D. Hawatmeh, A. Ross, K. Church, and T. M. Weller, "Characterization and modeling of K-band coplanar waveguides digitally manufactured using pulsed picosecond laser machining of thick-film conductive paste," *IEEE Transactions on Microwave Theory and Techniques*, vol. 65, no. 9, pp. 3180–3187, 2017.

[3] S. Y. Jun, B. Sanz-Izquierdo, E. A. Parker, D. Bird, and A. McClelland, "Manufacturing considerations in the 3-D printing of fractal antennas," *IEEE Transactions on Components, Packaging and Manufacturing Technology*, vol. 7, no. 11, pp. 1891–1898, 2017.

[4] K. Johnson, M. Zemba, B. P. Conner, J. Walker, E. Burden, K. Rogers, K. R. Cwiok, E. Macdonald, and P. Cortes, "Digital manufacturing of pathologically-complex 3D printed antennas," *IEEE Access*, vol. 7, pp. 39 378–39 389, 2019.

[5] M. Liang, C. Shemelya, E. MacDonald, R. Wicker, and H. Xin, "3-D printed microwave patch antenna via fused deposition method and ultrasonic wire mesh embedding technique," *IEEE Antennas and Wireless Propagation Letters*, vol. 14, pp. 1346–1349, 2015.

[6] M. I. M. Ghazali, S. Karuppuswami, S. Mondal, A. Kaur, and P. Chahal, "Embedded actives using additive manufacturing for high-density RF circuits and systems," *IEEE Transactions on Components, Packaging and Manufacturing Technology*, vol. 9, no. 8, pp. 1643–1651, 2019.

[7] B. K. Tehrani, B. S. Cook, and M. M. Tentzeris, "Inkjet printing of multilayer millimeter-wave yagi-uda antennas on flexible substrates," *IEEE Antennas and Wireless Propagation Letters*, vol. 15, pp. 143–146, 2016.

[8] D. F. Hawatmeh, S. LeBlanc, P. I. Deffenbaugh, and T. Weller, "Embedded 6-GHz 3-D printed half-wave dipole antenna," *IEEE Antennas and Wireless Propagation Letters*, vol. 16, pp. 145–148, 2017.

[9] P. Pa, Z. Larimore, P. Parsons, and M. Mirotznik, "Multi-material additive manufacturing of embedded low-profile antennas," *Electronics Letters*, vol. 51, no. 20, pp. 1561–1562, 2015.

[10] G. McKerricher, D. Titterington, and A. Shamim, "A fully inkjet-printed 3-D honeycomb-inspired patch antenna," *IEEE Antennas and Wireless Propagation Letters*, vol. 15, pp. 544–547, 2016.

[11] E. García-Marín, J. L. Masa-Campos, P. Sánchez-Olivares, and J. A. Ruiz-Cruz, "Evaluation of additive manufacturing techniques applied to Ku-band multilayer corporate waveguide antennas," *IEEE Antennas and Wireless Propagation Letters*, vol. 17, no. 11, pp. 2114–2118, 2018.

[12] T. Chio, G. Huang, and S. Zhou, "Application of direct metal laser sintering to waveguide-based passive microwave components, antennas, and antenna arrays," *Proceedings of the IEEE*, vol. 105, no. 4, pp. 632–644, 2017.

[13] T. P. Ketterl, Y. Vega, N. C. Arnal, J. W. I. Stratton, E. A. Rojas-Nastrucci, M. F. Córdoba-Erazo, M. M. Abdin, C. W. Perkowski, P. I. Deffenbaugh, K. H. Church, and T. M. Weller, "A 2.45 GHz phased array antenna unit cell fabricated using 3-D multi-layer direct digital manufacturing," *IEEE Transactions on Microwave Theory and Techniques*, vol. 63, no. 12, pp. 4382–4394, 2015.

[14] M. Kacar, C. Perkowski, P. Deffenbaugh, J. Booth, G. Mumcu, and T. Weller, "Wideband Ku-band antennas using multi-layer direct digital manufacturing," in *2017 IEEE International Symposium on Antennas and Propagation & USNC/URSI National Radio Science Meeting*, Conference Proceedings, pp. 1243–1244.

[15] M. Kacar, "Direct digital manufacturing of multi-layer wideband Ku-band patch antennas," Thesis, 2017.

[16] R. Sorrentino, P. Martin-Iglesias, O. A. Peverini, and T. M. Weller, "Additive manufacturing of radio-frequency components [scanning the issue]," *Proceedings of the IEEE*, vol. 105, no. 4, pp. 589–592, 2017.

[17] M. Kacar, T. M. Weller, and G. Mumcu, "3D printed wideband multilayered dual-polarized stacked patch antenna with integrated MMIC switch," *IEEE Open Journal of Antennas and Propagation*, pp. 1–1, 2020.

[18] P. I. Deffenbaugh, "3D printed electromagnetic transmission and electronic structures fabricated on a single platform using advanced process integration techniques," Thesis, 2014.

[19] S. Moscato, R. Bahr, T. Le, M. Pasian, M. Bozzi, L. Perregrini, and M. M. Tentzeris, "Infill-dependent 3-D-printed material based on ninjaflex filament for antenna applications," *IEEE Antennas and Wireless Propagation Letters*, vol. 15, pp. 1506–1509, 2016.

[20] J. S. Silva, M. García-Vigueras, T. Debogović, J. R. Costa, C. A. Fernandes, and J. R. Mosig, "Stereolithography-based antennas for satellite communications in Ka-band," *Proceedings of the IEEE*, vol. 105, no. 4, pp. 655–667, 2017.

[21] M. v. d. Vorst and J. Gumpinger, "Applicability of 3D printing techniques for compact ku-band medium/high-gain antennas," in *2016 10th European Conference on Antennas and Propagation (EuCAP)*, Conference Proceedings, pp. 1–4.

[22] H. H. Sigmarsson, E. C. Kinzel, X. Xu, and W. J. Chappell, "Selective laser sintering of multilayer, multimaterial circuit components," in *2006 IEEE MTT-S International Microwave Symposium Digest*, Conference Proceedings, pp. 1788–1791.

[23] M. Ramadan and R. Dahle, "Characterization of 3-D printed flexible heterogeneous substrate designs for wearable antennas," *IEEE Transactions on Antennas and Propagation*, vol. 67, no. 5, pp. 2896–2903, 2019.

[24] E. Massoni, L. Silvestri, G. Alaimo, S. Marconi, M. Bozzi, L. Perregrini, and F. Auricchio, "3-D printed substrate integrated slab waveguide for single-mode bandwidth enhancement," *IEEE Microwave and Wireless Components Letters*, vol. 27, no. 6, pp. 536–538, 2017.

[25] J. E. Chan, K. Sivaprasad, and K. A. Chamberlin, "High-frequency modeling of frequency-dependent dielectric and conductor losses in transmission lines," *IEEE Transactions on Components and Packaging Technologies*, vol. 30, no. 1, pp. 86–91, 2007.

[26] A. Ghannam, C. Viallon, D. Bourrier, and T. Parra, "Dielectric microwave characterization of the SU-8 thick resin used in an above IC process," in *2009 European Microwave Conference (EuMC)*, Conference Proceedings, pp. 1041–1044.

[27] M. Abt, A. Roch, J. A. Qayyum, S. Pestotnik, L. Stepien, A. Abu-Ageel, B. Wright, A. C. Ulusoy, J. Albrecht, L. Harle, J. Papapolymerou, and T. Schuelke, "Aerosol-printed highly conductive Ag transmission lines for flexible electronic devices," *IEEE Transactions on Components, Packaging and Manufacturing Technology*, vol. 8, no. 10, pp. 1838–1844, 2018.

[28] J. W. Stratton, "A study of direct digital manufactured rf/microwave packaging," Thesis, 2015.

[29] K. H. Church, N. B. Crane, P. I. Deffenbaugh, T. P. Ketterl, C. G. Neff, P. B. Nesbitt, J. T. Nussbaum, C. Perkowski, H. Tsang, J. Castro, J. Wang, and T. M. Weller, "Multimaterial and multilayer direct digital manufacturing of 3-D structural microwave electronics," *Proceedings of the IEEE*, vol. 105, no. 4, pp. 688–701, 2017.

[30] F. Cai, Y. Chang, K. Wang, C. Zhang, B. Wang, and J. Papapolymerou, "Low-loss 3-D multilayer transmission lines and interconnects fabricated by additive manufacturing technologies," *IEEE Transactions on Microwave Theory and Techniques*, vol. 64, no. 10, pp. 3208–3216, 2016.

[31] B. K. Tehrani, J. Bito, B. S. Cook, and M. M. Tentzeris, "Fully inkjet-printed multilayer microstrip and T-resonator structures for the RF characterization of printable materials and interconnects," in *2014 IEEE MTT-S International Microwave Symposium (IMS2014)*, Conference Proceedings, pp. 1–4.

[32] P. I. Deffenbaugh, T. M. Weller, and K. H. Church, "Fabrication and microwave characterization of 3-D printed transmission lines," *IEEE Microwave and Wireless Components Letters*, vol. 25, no. 12, pp. 823–825, 2015.

[33] M. I. M. Ghazali, S. Karuppuswami, A. Kaur, and P. Chahal, "3-D printed air substrates for the design and fabrication of RF components," *IEEE Transactions on Components, Packaging and Manufacturing Technology*, vol. 7, no. 6, pp. 982–989, 2017.

[34] S. D. Targonski, R. B. Waterhouse, and D. M. Pozar, "Design of wide-band aperture-stacked patch microstrip antennas," *IEEE Transactions on Antennas and Propagation*, vol. 46, no. 9, pp. 1245–1251, 1998.

[35] C. H. Tsao, Y. M. Hwang, F. Kilburg, and F. Dietrich, "Aperture-coupled patch antennas with wide-bandwidth and dual-polarization capabilities," in *1988 IEEE AP-S. International Symposium, Antennas and Propagation*, Conference Proceedings, pp. 936–939 vol.3.

[36] M. Yamazaki, E. T. Rahardjo, and M. Haneishi, "Construction of a slot-coupled planar antenna for dual polarisation," *Electronics Letters*, vol. 30, no. 22, pp. 1814–1815, 1994.

[37] M. Kacar, C. Perkowski, K. Church, B. Wu, J. Wang, T. Weller, and G. Mumcu, "Phased array antenna element with embedded cavity and MMIC using direct digital manufacturing," in *2019 IEEE International Symposium on Antennas and Propagation & USNC/URSI National Radio Science Meeting*, Conference Proceedings.

[38] X. Yu, M. Liang, C. Shemelya, D. A. Roberson, R. Wicker, E. MacDonald, and H. Xin, "3-D printed parts for a multilayer phased array antenna system," *IEEE Antennas and Wireless Propagation Letters*, vol. 17, no. 11, pp. 2150–2154, 2018.

[39] R. A. Ramirez, D. Lan, J. Wang, and T. M. Weller, "MMIC packaging and on-chip low-loss lateral interconnection using additive manufacturing and laser machining," in *2017 IEEE MTT-S International Microwave Symposium (IMS)*, Conference Proceedings, pp. 38–40.

[40] R. L. Haupt and Y. Rahmat-Samii, "Antenna array developments: A perspective on the past, present and future," *IEEE Antennas and Propagation Magazine*, vol. 57, no. 1, pp. 86–96, 2015.

[41] J. S. Herd and M. D. Conway, "The evolution to modern phased array architectures," *Proceedings of the IEEE*, vol. 104, no. 3, pp. 519–529, March 2016.

[42] M. Oppermann and R. Rieger, "Multifunctional MMICs – key enabler for future AESA panel arrays," in *2018 IMAPS Nordic Conference on Microelectronics Packaging (NordPac)*, 2018, pp. 77–80.

[43] K. J. Byers and C. Barr, "Metal additive manufactured freeform antenna," *IEEE Antennas and Wireless Propagation Letters*, vol. 17, no. 11, pp. 2104–2108, 2018.

[44] D. González-Ovejero, N. Chahat, R. Sauleau, G. Chattopadhyay, S. Maci, and M. Ettorre, "Additive manufactured metal-only modulated metasurface antennas," *IEEE Transactions on Antennas and Propagation*, vol. 66, no. 11, pp. 6106–6114, 2018.

[45] E. A. Rojas-Nastrucci, J. T. Nussbaum, N. B. Crane, and T. M. Weller, "Ka-band characterization of binder jetting for 3-D printing of metallic rectangular waveguide circuits and antennas," *IEEE Transactions on Microwave Theory and Techniques*, vol. 65, no. 9, pp. 3099–3108, 2017.

[46] M. F. Farooqui and A. Shamim, "3-D inkjet-printed helical antenna with integrated lens," *IEEE Antennas and Wireless Propagation Letters*, vol. 16, pp. 800–803, 2017.

[47] B. S. Cook, B. Tehrani, J. R. Cooper, and M. M. Tentzeris, "Multilayer inkjet printing of millimeter-wave proximity-fed patch arrays on flexible substrates," *IEEE Antennas and Wireless Propagation Letters*, vol. 12, pp. 1351–1354, 2013.

[48] S. Y. Jun, A. Elibiary, B. Sanz-Izquierdo, L. Winchester, D. Bird, and A. McCleland, "3-D printing of conformal antennas for diversity wrist worn applications," *IEEE Transactions on Components, Packaging and Manufacturing Technology*, vol. 8, no. 12, pp. 2227–2235, 2018.

[49] M. Kacar, T. M. Weller, and G. Mumcu, "Conductivity improvement of microdispensed microstrip lines and grounded coplanar waveguides using laser micromachining," *IEEE Transactions on Components, Packaging and Manufacturing Technology*, pp. 1–1, 2020.

[50] A. I. Dimitriadis, T. Debogović, M. Favre, M. Billod, L. Barloggio, J. Ansermet, and E. de Rijk, "Polymer-based additive manufacturing of high-performance waveguide and antenna components," *Proceedings of the IEEE*, vol. 105, no. 4, pp. 668–676, 2017.

[51] A. A. Nawaz, W. T. Khan, and A. C. Ulusoy, "Organically packaged components and modules: Recent advancements for microwave and mm-wave applications," *IEEE Microwave Magazine*, vol. 20, no. 11, pp. 49–72, 2019.

[52] A. Eid, X. He, R. Bahr, T. H. Lin, Y. Cui, A. Adeyeye, B. Tehrani, and M. M. Tentzeris, "Inkjet-/3D-/4D-printed perpetual electronics and modules: RF and mm-Wave devices for 5G+, IoT, smart agriculture, and smart cities applications," *IEEE Microwave Magazine*, vol. 21, no. 12, pp. 87–103, 2020.

[53] B. K. Tehrani, B. S. Cook, and M. M. Tentzeris, "Inkjet-printed 3D interconnects for millimeter-wave system-on-package solutions," in *2016 IEEE MTT-S International Microwave Symposium (IMS)*, 2016, pp. 1–4.

[54] M. I. M. Ghazali, S. Karuppuswami, S. Mondal, A. Kaur, and P. Chahal, "Embedded actives using additive manufacturing for high-density RF circuits and systems," *IEEE Transactions on Components, Packaging and Manufacturing Technology*, vol. 9, no. 8, pp. 1643–1651, 2019.

[55] C. Oakley, J. D. Albrecht, J. Papapolymerou, and P. Chahal, "Low-loss aerosol-jet printed wideband interconnects for embedded devices," *IEEE Transactions on Components, Packaging and Manufacturing Technology*, vol. 9, no. 11, pp. 2305–2313, 2019.

[56] X. He, B. K. Tehrani, R. Bahr, W. Su, and M. M. Tentzeris, "Additively manufactured mm-wave multichip modules with fully printed "smart" encapsulation structures," *IEEE Transactions on Microwave Theory and Techniques*, vol. 68, no. 7, pp. 2716–2724, 2020.

[57] M. T. Craton, X. Konstantinou, J. D. Albrecht, P. Chahal, and J. Papapolymerou, "A chip-first microwave package using multimaterial aerosol jet printing," *IEEE Transactions on Microwave Theory and Techniques*, vol. 68, no. 8, pp. 3418–3427, 2020.

[58] J. G. Hester, S. Kim, J. Bito, T. Le, J. Kimionis, D. Revier, C. Saintsing, W. Su, B. Tehrani, A. Traille, B. S. Cook, and M. M. Tentzeris, "Additively manufactured nanotechnology and origami-enabled flexible microwave electronics," *Proceedings of the IEEE*, vol. 103, no. 4, pp. 583–606, 2015.

[59] M. Rizwan, A. A. Kutty, M. Kgwadi, T. D. Drysdale, L. Sydänheimo, L. Ukkonen, and J. Virkki, "Possibilities of fabricating copper-based RFID tags with photonic-sintered inkjet printing and thermal transfer printing," *IEEE Antennas and Wireless Propagation Letters*, vol. 16, pp. 1828–1831, 2017.

[60] J. Niittynen and M. Mäntysalo, "Characterization of laser sintering of copper nanoparticle ink by FEM and experimental testing," *IEEE Transactions on Components, Packaging and Manufacturing Technology*, vol. 4, no. 12, pp. 2018–2025, 2014.

[61] C. E. Hajjaji, J. George, S. Lmansouri, N. Delhote, S. Verdeyme, D. Baillargeat, M. Piechowiak, and O. Durand, "Optimizing the conductivity of ink-jet printed microwave components on polymer substrates by laser sintering," in *2019 49th European Microwave Conference (EuMC)*, Conference Proceedings, pp. 778–781.

[62] A. A. Gupta, M. C. M. Soer, M. Taherzadeh-Sani, S. G. Cloutier, and R. Izquierdo, "Aerosol-jet printed transmission lines for microwave packaging applications," *IEEE Transactions on Components, Packaging and Manufacturing Technology*, vol. 9, no. 12, pp. 2482–2489, 2019.

[63] B. S. Cook and A. Shamim, "Inkjet printing of novel wideband and high gain antennas on low-cost paper substrate," *IEEE Transactions on Antennas and Propagation*, vol. 60, no. 9, pp. 4148–4156, 2012.

[64] P. Escobedo, M. A. Carvajal, J. Banqueri, A. Martínez-Olmos, L. F. Capitán-Vallvey, and A. J. Palma, "Comparative study of inkjet-printed silver conductive traces with thermal and electrical sintering," *IEEE Access*, vol. 7, pp. 1909–1919, 2019.

[65] M. M. Abdin, W. J. D. Johnson, J. Wang, and T. M. Weller, "W-band finite ground coplanar waveguide (FG-CPW) using laser enhanced direct-print additive manufacturing (LE-DPAM)," in *2019 IEEE MTT-S International Microwave Symposium (IMS)*, Conference Proceedings, pp. 1213–1216.

[66] C. Neff, E. A. Rojas-Nastrucci, J. Nussbaum, D. Griffin, T. M. Weller, and N. B. Crane, "Thermal and vapor smoothing of thermoplastic for reduced surface roughness of additive manufactured RF electronics," *IEEE Transactions on Components, Packaging and Manufacturing Technology*, vol. 9, no. 6, pp. 1151–1160, 2019.

[67] E. A. Rojas-Nastrucci, R. A. Ramirez, and T. M. Weller, "Direct digital manufacturing of mm-wave vertical interconnects," in *2018 IEEE 19th Wireless and Microwave Technology Conference (WAMICON)*, 2018, pp. 1–3.

[68] S. Kim, A. Shamim, A. Georgiadis, H. Aubert, and M. M. Tentzeris, "Fabrication of fully inkjet-printed vias and SIW structures on thick polymer substrates," *IEEE Transactions on Components, Packaging and Manufacturing Technology*, vol. 6, no. 3, pp. 486–496, 2016.

[69] *Conformal Arrays.* John Wiley & Sons, Ltd, 2009, ch. 11, pp. 399–464. [Online]. Available: https://onlinelibrary.wiley.com/doi/abs/10.1002/9780470529188.ch11

Appendix A: Copyright Permissions

The permission above is for the use of materials in Chapter 3.

The permission above is for the use of materials in Chapter 5.

About the Author

Merve Kacar received B.Sc. degree in electrical and electronics engineering from the Middle East Technical University, Ankara, Turkey in 2015, and the M.Sc. degree in electrical engineering from the University of South Florida, Tampa, FL, USA, in 2017. She has obtained her Ph.D. degree in Reconfigurable RF Devices & Systems Laboratory (ReDS), which is part of Center for Wireless and Microwave Information Systems (WAMI). Her research is focused on additive manufacturing of transmission lines, antennas, antenna arrays and 3D structural packaging of integrated circuits. She has carried her research efforts under multiple research awards supported by Army Small Business Innovation Research (SBIR) Program , America Makes, and Air Force SBIR Program. Her publication record includes three journal articles and seven conferences presentations/papers. She participated as an RF design engineer in several RF companies such as SV Microwave, West Palm Beach, FL in 2015 and Smiths Interconnect, Tampa, FL in 2019, and Modelithics Inc. in 2020. She is a member of IEEE Antenna Propagation Society (AP-S), Microwave Theory and Techniques Society (MTT-S), and Association of Old Crows. She served as secretary, vice chair and chair in the USF IEEE Student Branch Chapter of MTT-S.